



**Michigan
Technological
University**

Michigan Technological University
Digital Commons @ Michigan Tech

Dissertations, Master's Theses and Master's Reports

2019

MULTI-SCALE, CAPILLARY ASSISTED COPPER SURFACES FOR ENHANCED POOL BOILING HEAT TRANSFER PROCESSES

Chetan Agarwal

Michigan Technological University, cagarwal@mtu.edu

Copyright 2019 Chetan Agarwal

Recommended Citation

Agarwal, Chetan, "MULTI-SCALE, CAPILLARY ASSISTED COPPER SURFACES FOR ENHANCED POOL BOILING HEAT TRANSFER PROCESSES", Open Access Master's Thesis, Michigan Technological University, 2019.

<https://doi.org/10.37099/mtu.dc.etr/862>

Follow this and additional works at: <https://digitalcommons.mtu.edu/etr>



Part of the [Heat Transfer, Combustion Commons](#), and the [Manufacturing Commons](#)

MULTI-SCALE, CAPILLARY ASSISTED COPPER SURFACES FOR ENHANCED
POOL BOILING HEAT TRANSFER PROCESSES

By

Chetan Sanjay Agarwal

A THESIS

Submitted in partial fulfillment of the requirements for the degree of

MASTER OF SCIENCE

In Mechanical Engineering

MICHIGAN TECHNOLOGICAL UNIVERSITY

2019

© 2019 Chetan Sanjay Agarwal

This thesis has been approved in partial fulfillment of the requirements for the Degree of MASTER OF SCIENCE in Mechanical Engineering.

Department of Mechanical Engineering – Engineering Mechanics

Thesis Advisor: *Dr. Sajjad Bigham*

Committee Member: *Dr. Kazuya Tajiri*

Committee Member: *Dr. Song-Lin Yang*

Department Chair: *Dr. William W. Predebon*

Table of Contents

List of figures.....	v
List of tables.....	ix
Preface.....	x
Acknowledgements.....	xi
Definitions.....	xii
List of abbreviations	xiii
Abstract.....	xiv
1 Introduction.....	1
1.1 Boiling Curve	3
1.2 Bubble Nucleation.....	6
1.3 Heat Transfer Model	8
2 Literature Review.....	10
2.1 Heat Transfer enhancement strategies in Pool Boiling	10
2.1.1 Structured surfaces.....	10
2.1.2 Porous Structures	14
2.1.2.1 Coating.....	14
2.1.2.2 Chemical Treatment.....	16
2.1.2.3 Sintering.....	17
2.1.2.4 Nanowires	19
2.1.3 Hybrid Structures.....	21
2.1.3.1 Modulated Structures.....	21
2.1.3.2 Hierarchical structure.....	23
3 Objective and Concept of this research	26
3.1 Augmented Roughness.....	30
3.2 Promoted liquid supply	31
3.3 Decoupled liquid/vapor pathways	32
4 Fabrication	35
4.1 Fabrication of test samples	35
4.1.1 Diffusion bonding.....	35
4.1.2 Machining of Test samples	37

4.1.3	Acid Cleaning	39
4.1.4	Nanowire growth	39
4.1.4.1	Acid Washing.....	40
4.1.4.2	Chemical Treatment.....	40
4.2	Fabrication of the experimental setup	41
4.2.1	Heating block and 1D column	41
4.2.2	Acrylic Tube and O rings.....	43
4.2.3	Mounting Plates	43
4.2.4	Condenser, chiller and rope heaters	45
4.2.5	Electrical devices	45
5	Experimental setup and data analysis	49
5.1	Experimental procedure	49
5.2	Data Analysis	51
5.3	Uncertainty Analysis	52
6	Results and Discussion	57
6.1	Effect of out-of-plane capillary wicking length scale on heat transfer performance.	57
6.1.1	Effect of out-of-plane capillary wicking length scale on heat flux...58	
6.1.2	Effect of out-of-plane capillary wicking length scale on heat transfer coefficient.....60	
6.2	Effect of growth of hierarchical structures on heat transfer performance.....61	
6.2.1	Effect of test sample H_1 and $H_{1,NW}$ with and without nanowires on heat flux.....61	
6.2.2	Effect of test sample H_2 and $H_{2,NW}$ with and without nanowires on heat flux.....63	
6.2.3	Effect of test sample $H_{1,NW}$ and $H_{2,NW}$ on heat transfer coefficient.66	
7	Conclusion	67
8	Future Scope	68
9	Reference List	69
A	Calculations.....	75
A.1	Calculation of Heat flux as predicted by Rohsenov model	75
A.2	Calculation of maximum heat flux as predicted by Kutateladze and Zuber ..75	
B	Copyright documentation.....	78

List of figures

Figure 1.1: Plot indicating typical HTC for different cooling mediums [15].....	2
Figure 1.2: Typical Pool boiling curve	4
Figure 1.3: Vapor bubble in a cavity of size R depicting vapor/liquid pressure across it. ..	6
Figure 1.4: Different heat transfer mechanism during a) bubble nucleation b) bubble departure (Copyright of Kim et al. [33]).....	8
Figure 2.1: SEM images of three different micro-pin structures with increasing height. (Copyright of Wei and Honda [36]).....	12
Figure 2.2: SEM images of differently spaced square pin-fins with magnified view (Copyright of Zhang & Lian [37]).....	12
Figure 2.3: SEM images of six different configurations of silicon etched micropillars with all three dimension variation (Copyright of Chu et al. [38]).	13
Figure 2.4: Differently spaced SEM images of micro-pin-fin silicon chip (Copyright of Kim et al. [39]).....	13
Figure 2.5: 3d profiler image of the simulated micro pillared sampled surface (Copyright of Kim et al. [40]).	13
Figure 2.6: SEM image of 0.01 inch diameter nickel wire coated with 40 bilayers of polymer/SiO ₂ (Copyright of Forrest et al. [41]).....	15
Figure 2.7: SEM images of Platinum wire with 20 nm alumina coating with scale bar as 2 μm (Copyright of Feng et al. [42]).....	15
Figure 2.8: SEM images of Cu dendritic growth forming microporous surfaces with HR-SEM and TEM images (bottom two) of the Cu deposition peeled off from the surface (Copyright of Li et al. [44]).....	17
Figure 2.9: Alumina porous structure formed at two different electrolytic voltage (left) with their cross sectional view (right) (Copyright of Zhang et al. [45]).....	17
Figure 2.10: (a) SEM image of the self assembled 3D porous structure formed via reduced graphene (b) schematic representing the porous structure layering (Copyright of Ahn et al. [46]).....	17
Figure 2.11: Images of unit cell representation (top) and fabricated copper foam matrices with different porosity (bottom) (Copyright of Wong & Leong [49]).....	18

Figure 2.12: SEM images of top view (left) and cross sectional view (right) of Silicon (top) and Copper (bottom) nanowires respectively (Copyright of Chen et al. [50]).	20
Figure 2.13: FESEM images of nanowires indicating top view, diameter and height (left to right) for Copper (top) and Silver (bottom) respectively (Copyright of Kumar et al. [52]).	21
Figure 2.14: SEM images of modulated hybrid structures by three different research groups. (I) Geometric representation of porous structures with re-entrant cavities at three different magnification from left to right (Copyright of Deng et al. [53]). (II) SEM images of porous modulated structures fabricated from spherical copper particles indicating side view, top view and perspective view from left to right respectively (Copyright of Liter and Kaviany [54]). (III) SEM images of modulated porous structures of 500 μm thickness and 250 μm particle size (Copyright of Li et al.[55]).	23
Figure 2.15: SEM images of Silicon (top) and Copper oxide (bottom) based hierarchical surfaces with magnified view from left to right (Copyright of Chu et al.[56]).	25
Figure 2.16: SEM images of the four different microstructure samples (left to right) with hierarchical surfaces grown on them. Each columns indicating three different magnifications levels (Copyright of Rahman et al. [57]).	25
Figure 2.17: SEM images of (a) micro textured surface with plain square micropillar (b) nano textured micropillar covered with nanograss (Copyright of Dhillon et al. [58]).	25
Figure 3.1: Graph indicating the objective of the research to enhance CHF while simultaneously reducing the excess temperature.	26
Figure 3.2: Test sample surface geometry schematic of the designed surface topology.	29
Figure 3.3: Test sample surface geometry Image of the actual fabricated test sample with dimensions	29
Figure 3.4: Schematic representation of top: sample under test before CHF and bottom: sample under test during CHF.	30
Figure 3.5: Schematic indicating additional nucleation because of formation of micropores due to meshed structures	31
Figure 3.6: Schematic showing the momentum forces acting on bubble on (a) plain surface (b) corner of channel and (c) flow of liquid across a fin (Copyright of Kandlikar et al. [59]).	33

Figure 3.7: Schematic representation liquid pathway through the mesh while vapor escaping from the sides of the meshed structures.	34
Figure 4.1: Image showing the copper substrate and the copper meshed after cleaning them, ready for diffusion bonding	36
Figure 4.2: Sample after diffusion bonding	37
Figure 4.3: Final machined test sample	38
Figure 4.4: Microscopic images of the test sample with top: cross sectional view and bottom: plan view with enlarged pillar image	39
Figure 4.5: SEM images of the micro-structured pillar at different magnification level. .	41
Figure 4.6: 3D CAD model representing the heating block with 1D column.	43
Figure 4.7: 3D CAD model of Bottom mounting plate.	44
Figure 4.8: 3D CAD model of Top mounting plate.....	45
Figure 4.9: Power source for cartridge heater, VARIAC	46
Figure 4.10: Agilent DAQ system	46
Figure 4.11: Exploded view of the final assembled 3D CAD model of the experimental test setup.....	47
Figure 4.12: Schematic of Test setup with different sub components.....	48
Figure 5.1: Image of the assembled test setup.	50
Figure 5.2: Thermocouple location in the 1D column.....	51
Figure 5.3: Graph indicating the percentage uncertainty at different heat flux values.....	56
Figure 6.1: Heat flux as a function of wall superheat at different out-of-plane capillary wicking length scales.	58
Figure 6.2: Heat transfer coefficient versus heat flux.....	60
Figure 6.3: Heat flux as a function of wall superheat for the test samples H_1 and $H_{1, NW}$. 61	
Figure 6.4a: Heat flux versus wall superheat for the test sample H_2 , $H_{2, NW}$, and plain surfaces.	63

Figure 6.4b: Heat flux versus wall superheat for the test sample $H_{1,NW}$, $H_{2,NW}$, and plain surfaces.63

Figure 6.5: Heat transfer coefficient versus wall superheat for the test samples with nanowires $H_{1,NW}$ and $H_{2,NW}$66

List of tables

Table 4.1: Specification of the inter-woven copper meshed onto the substrate	37
Table 5.1: Values of uncertainties in various parameters	54

Preface

The introduction and literature review sections of this document includes images from formerly published articles. The images are included to provide a better understanding of the motivation and research direction of enhancing pool boiling over a course of time. The images are sole authority of the respective authors and none have been reproduced in this study by any means. Due credit of the original articles has been provided as citations and official permission has been taken beforehand for each image to be referred in this thesis.

Acknowledgements

I am fortunate and deeply thankful to my mentor and advisor, Dr. Sajjad Bigham, for introducing me to the field of thermal management and heat transfer studies. I am truly grateful to him for giving me the opportunity to conduct my research under his guidance. He has always been a fundamental source of inspiration throughout the entirety of this thesis, from concept introduction to final goal realization. Insights and learnings gained from him will surely help me to realize my future goals.

I would also like to thank my former and current lab partners at EnergyX, the MEEM machine shop faculty, Mr. Martin Toth and Mr. Jonathan Lund, for helping me throughout the fabrication steps. Their expertise helped me overcome the complex fabrication stage of my research.

Lastly, I give my humblest gratitude to my family for their constant, unconditional love and support throughout my life. They are my foremost source of inspiration to pursue greater good and knowledge in my life. I am eternally thankful to them.

Definitions

$\Delta T_{sat} = T_{surface} - T_{sat} = \text{wall superheat/excess temperature } (^\circ\text{C})$

T_{sat} saturation temperature of the working fluid ($^\circ\text{C}$)

$T_{surface}$ surface temperature of the test sample ($^\circ\text{C}$)

q'' heat flux (W/cm^2)

R cavity size (m)

P_v vapor pressure (N/m^2)

P_l liquid pressure (N/m^2)

σ surface tension of the liquid (N/m)

δt thermal boundary layer thickness (μm)

Θ contact angle of the liquid with solid substrate ($^\circ\text{C}$)

Θ_r receding contact angle of the liquid with solid substrate ($^\circ\text{C}$)

h_{lg} latent heat of liquid to vapor $A = (\text{kJ}/\text{kg} - \text{K})$

q_{mc} heat flux due to micro-convection (W/cm^2)

q_{ml} heat flux due to microlayer evaporation (W/cm^2)

q_{cl} heat flux due to thin film/contact line evaporation (W/cm^2)

q_{nc} heat flux due to natural convection (W/cm^2)

k_{cu} thermal conductivity of Copper ($\text{W}/\text{m} - \text{K}$)

S_y Systematic/Bias error

R_y Random/Precision error

h heat transfer coefficient ($\text{W}/\text{cm}^2 - \text{K}$)

List of abbreviations

<i>ID</i>	<i>One Dimensional</i>
<i>CHF</i>	<i>Critical Heat Flux</i>
<i>HTC</i>	<i>Heat Transfer Coefficient</i>
<i>MEMS</i>	<i>Micro Electro Mechanical Systems</i>
<i>ONB</i>	<i>Onset of Nucleate Boiling</i>
<i>DI</i>	<i>De- Ionized</i>
<i>IPA</i>	<i>Isopropyl Alcohol</i>
<i>ipm</i>	<i>Inch per minute</i>
<i>rpm</i>	<i>rotations per minute</i>

Abstract

Phase-change heat transfer through pool boiling process offers a promising thermal management solution in applications wherein conventional air or single-phase liquid-based cooling methods prove inefficient such as for high-power electronics. Pool boiling process, which utilizes the latent heat of evaporation, provides a robust and efficient way to efficiently dissipate the excessive heat generated in a small footprint area in particular as seen in CPUs (Central Processing Units), GPUs (Graphics Processing Units), LEDs (Light Emitting Diodes), radars, and other demanding computing, sensing and surveillance electronics. Although boiling process has been studied for over five decades, it has not been yet adapted for widespread deployment. This is mainly due to the lack of a reliable high-performance boiling surface with exceptional heat dissipation potential. Boiling heat transfer is fundamentally limited by CHF (Critical Heat Flux), which is the maximum heat flux a given boiling surface can dissipate. At this point, a vapor layer covers the boiling surface causing surface temperature overshoot with a potential catastrophic failure. Deploying various active and passive methods, researchers have proposed different strategies to push further the CHF values, and thus widen the safe operating limits of a system. In this study, we propose a unique, passive surface topology to enhance heat transfer by altering three distinctive surface properties: augmented roughness, out-of-plane capillary wicking and separate liquid vapor pathways.

Firstly, a porous surface medium is introduced onto the boiling surface using copper mesh and diffusion bonding process. These bonded coppers meshes institutes a complex porous matrix structure which amplifies nucleation site density. The intertwined copper meshes

stacked and bonded atop each other forms guideways which provided preferential, out-of-plane capillary wicking supplementing liquid to the heater surface, in addition to in plane wicking. In addition, the copper meshes are machined into pillars which serves as a separate liquid-vapor pathway reducing the vapor escape resistance aiding in delaying CHF. Two surfaces with different number of coppers meshes were diffusion bonded and machined to study the effect of altered surface topology and out-of-plane capillary wicking length scale effect on heat transfer process.

Secondly, to further enhance heat transfer, the samples were chemically treated to grow nanowires on them. With the introduction of nanowire, hierarchical structures were prepared and studied for heat transfer performance enhancement. The best performing sample resulted into a record Critical Heat Flux of 475 W/cm^2 and heat transfer coefficient $70.8 \text{ W/cm}^2\text{K}$. These are about 3.7 times and about 14 times higher in heat flux and heat transfer coefficient as compared to a plain copper surface, respectively.

1 Introduction

Pool boiling is a heat transfer process which involves phase change at the liquid-vapor interface occurring at saturation temperature. Because boiling involves phase change heat transfer, it utilizes the latent heat of a fluid and thus is considered one of the most efficient heat transfer process. Boiling plays a very critical role in processes involving very high heat flux generation and extraction from a small area, such as electronic devices of very high-power density [1-4], servers/data centers [5-8], satellite and spacecraft avionics [9-11] and hybrid electric vehicle battery thermal management [12-14]. Conventional heat transfer mediums prove incapable of extracting such vast quantities of heat. Pool boiling establishes a very cost effective, passive cooling strategy as it involves no moving parts. In a general term, heat transfer coefficient (HTC) is an indication of how effectively heat is being transferred from a medium. Figure 1.1 shown below summarizes the HTC of different mediums highlighting how HTC for boiling is almost two orders of magnitude more as compared to air.

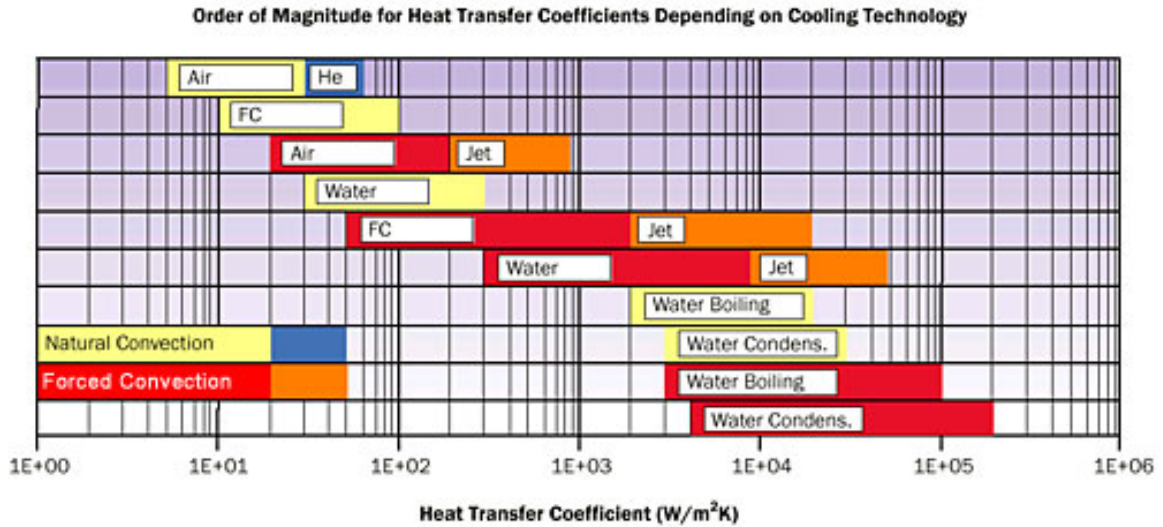


Figure 1.1: Plot indicating typical HTC for different cooling mediums [15]

Pool boiling is a type of phase change process wherein heat transfer occurs on the heater surface, via bubble formation, which is submerged in large pool of stagnant liquid. Although, the heat transfer for pool boiling is almost two orders of magnitude higher than the conventional cooling methods, it is still limited by Critical Heat Flux of about 100-150 W/cm² depending on the type of surface [16]. Critical heat flux is the maximum amount of heat flux a surface can transfer to liquid before a vapor layer covers the surface shooting its temperature to a very high value [17]. With increasing technological advancements, there is a growing demand to push the CHF limit to higher values [18]. Different research groups proposed various strategies to enhance boiling heat transfer performance [19].

1.1 Boiling Curve

Boiling heat transfer mechanism can be better explained with the help of boiling curve. Boiling curve is a plot of heat flux vs. wall superheat. Heat flux is the amount of heat extracted per unit area. Wall superheat is the difference between the surface temperature and liquid pool temperature, which is the saturation temperature of the fluid at the given operating pressure. Boiling curve was extensively studied and introduced by Nukiyama [20] in 1934. Nukiyama conducted a number of experiments with Nichrome wire and water as the working fluid and was first to come up with the boiling curve. A boiling curve facilitates proper understanding of different boiling regimes, and mechanisms affecting heat transfer performance of the system under study. It also aids in developing heat transfer models, and depicting critical parameters affecting heat transfer. A boiling curve can either be achieved by controlling the heat flux or controlling the wall superheat, which further dictates what happens to the boiling curve after it reaches to CHF. Figure 1.2 shows the boiling curve achieved using heat flux-controlled methodology.

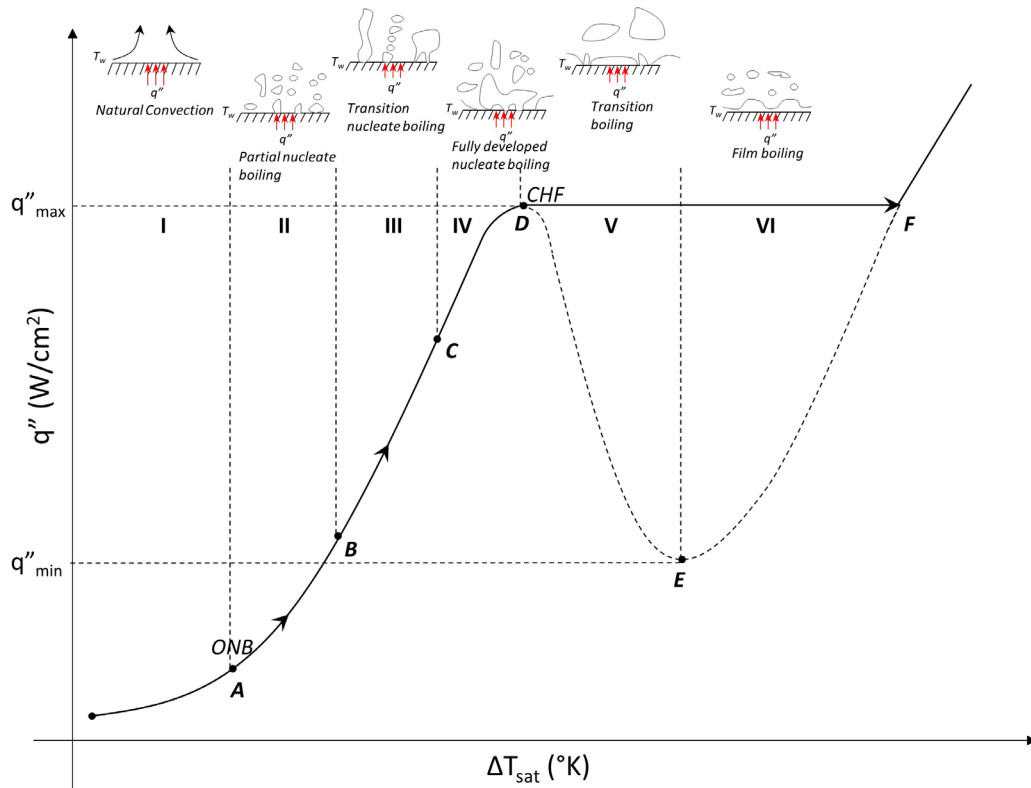


Figure 1.2: Typical Pool boiling curve

A typical boiling curve is divided into multiple regimes depicted by changes in trends of boiling curve due to the nature of bubble generation, its frequency and departure motion.

Typically, boiling curve has the following four distinct regimes [21, 22].

1. Single phase natural convection
2. Nucleate boiling
3. Transition boiling
4. Film boiling

As shown in Figure 1.2, up until the point A where the heater surface temperature is below the saturation temperature of the fluid, heat transfer is governed by single phase natural convection. Heat transfer is mainly by natural convection and therefore is linear in nature.

As the heat flux to the heater increases, the surface temperature rises and crosses the saturation temperature of the liquid pool. Only after the heater surface temperature passes a certain amount of superheat, one can see bubbles forming on the heater surface. This point A is known as Onset of Nucleate Boiling (ONB) and is governed by the size and number of cavities present on the surface. Nucleate boiling regime is further divided into three regimes, partial nucleate boiling (isolated bubble) regime, transition nucleate boiling (jets/column) regime and fully developed nucleate boiling regime. As heat flux increases, isolated bubble formation aids in extracting the excess heat flux resulting in increase in the slope of the graph.

Further increase in heat flux, beyond point B, activates more nucleation sites leading to an increase in bubble frequency which then coalesce to form jets and columns. After point C, due to increase in bubble generation frequency and resistance in vertical direction to vapor escape, bubbles expand and merge laterally leading to formation of vapor layer periodically covering the heater surface. The heat flux right before the vapor layer covers the heater surface entirely, is the maximum heat flux and is known as Critical Heat Flux (CHF) denoted by point D. Heat flux, beyond point D known as transition boiling, decreases as the HTC from vapor film is very less as compared to that of a liquid layer. It reaches a minimum value, known as Leidenfrost point E. After point E, a permanent vapor layer entirely covers the heater surface and heat flux increases beyond this point owing to radiation heat transfer mechanism dominating the cooling process.

1.2 Bubble Nucleation

Boiling occurs because of formation of bubble which is dependent on the size of the cavity. Cavities entrap air which serves as a starting nucleation point for bubbles to form, expand and then depart. For a bubble to expand and thus contribute towards heat transfer, the vapor pressure inside the bubble should be greater than the liquid pressure surrounding it. This difference in pressure is accounted by excess temperature of the heater surface from the saturation temperature of the pool of liquid. Figure 1.3 depicts the air entrapped in the cavity of size R.

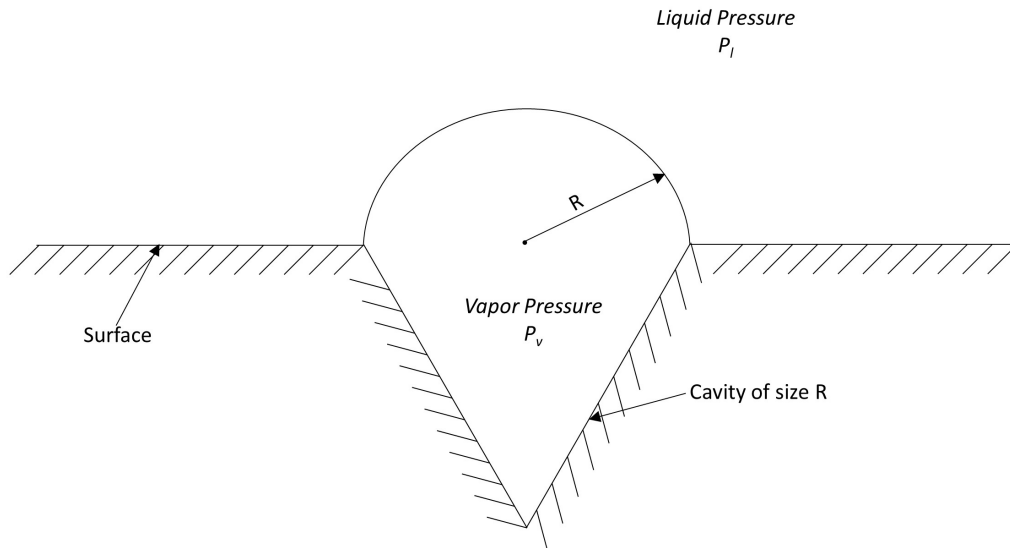


Figure 1.3: Vapor bubble in a cavity of size R depicting vapor/liquid pressure across it.

The vapor pressure inside the air entrapped bubble is given by

$$P_v = P_l + \frac{2\sigma}{R} \quad (1)$$

where, P_v = partial vapor pressure inside the bubble

P_l = liquid pressure surrounding the bubble

$\sigma = \text{surface tension of the vapor}$

$R = \text{radius of the cavity}$

Equation (1) specifies that the vapor (1) pressure is inversely proportional to the bubble radius. It gives the relationship between the cavity size and bubble nucleation. It also indicates that for a given wall superheat, in correspondence to heat flux, only a particular range of nuclei cavities gets activated [23]. The Equation (2) gives the range of radii activated for a given wall superheat.

$$R_{c,min}, R_{c,max} = \frac{\delta t \sin\theta}{2(1+\cos\theta_r)} * \left(\frac{\Delta T_{sat}}{\Delta T_{sat} + \Delta T_{sub}} \right) * \left(1 + \sqrt{1 - \frac{12.8 \sigma T_{sat} (\Delta T_{sat} + \Delta T_{sub})}{\rho_v h_{lg} \delta t \Delta T_{sat}^2}} \right) \quad (2)$$

If the superheat value decreases, the term inside the square root tends to zero and the above equation leads to $R_{c,min} = R_{c,max}$ leading to Equation (3) of critical radius value given by [23].

$$R_{c, \text{critical}} = \frac{\delta t \sin\theta}{2(1+\cos\theta_r)} * \left(\frac{\Delta T_{sat}}{\Delta T_{sat} + \Delta T_{sub}} \right) \quad (3)$$

Equation (3) implies that for a given wall superheat, only a particular size of cavity gets activated for nucleation. In general, for a wall superheat of 15 – 20 ° C, the range of critical radius cavities that gets activated is between ~ 1 μm and ~ 100 μm [24]. Therefore, to enhance the heat transfer by enhancing the nucleation site density, it is imperative to introduce cavities in the range of critical radius as depicted by the Equation (3) . The size and porosity of copper meshes were thus selected accordingly to introduce cavities within this desired range.

1.3 Heat Transfer Model

To better understand the heat transfer from the surface to the liquid and to conceptualize the parameters affecting the heat transfer, various models have been developed and put forth by researchers till date [25-31]. As discussed in the boiling curve, there are two prominent phenomena occurring during pool boiling, nucleate boiling and the occurrence of CHF. Therefore, to understand the physics behind the occurrence of nucleate boiling, factors affecting heat transfer and conditions leading to CHF can be better understood by these models [32].

In the nucleate boiling regime, heat transfer takes place through various mechanisms and correspondingly, each mechanism has its contribution to overall heat transfer. Figure 1.4 depicts the four prominent heat transfer mechanisms, transient conduction, micro-convection (q_{mc}), microlayer evaporation (q_{ml}) and thin film/contact line evaporation (q_{cl}) in addition to natural convection (q_{nc}) [31].

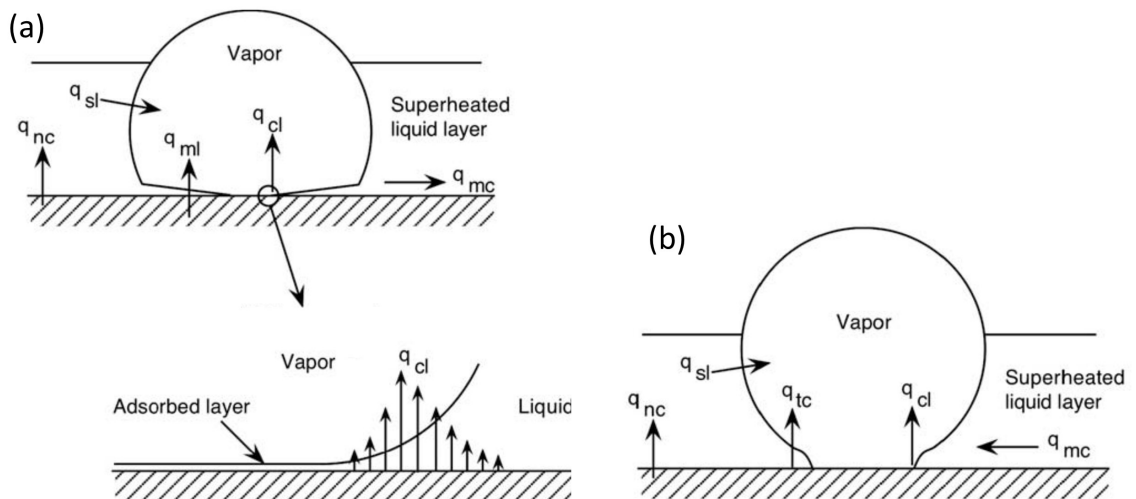


Figure 1.4: Different heat transfer mechanism during a) bubble nucleation b) bubble departure (Copyright of Kim et al. [33]).

The transient conduction assumes a pure conduction occurring because of rewetting of hot surface by the cool liquid replacing the departing bubble. Micro convection assumes heat transfer via bubble growth and departure incurred because of liquid motion induced by the wake of departing bubble. Micro-layer evaporation proposes the heat transfer occurs because of evaporation of microlayer on the surface. Lastly, the thin film evaporation or contact line evaporation, is the heat transfer because of evaporation of the thin liquid film at the three-phase contact line between the vapor bubble, liquid and the solid surface. It is postulated that the thin film evaporation dominates the nucleate boiling process [31]. Therefore, in order to enhance heat transfer, it is vital to understand and imply methodologies to improve thin film evaporation.

2 Literature Review

2.1 Heat Transfer enhancement strategies in Pool Boiling

In flow boiling, increase in flow velocity helps in sweeping bubble away from the surface thus delaying their coalescence and ultimately CHF. In contrast to flow boiling, pool boiling incorporates weak fluidic motion which is induced by buoyancy and bubble agitation. This weak motion is random and often uncontrolled. Therefore, enhancing heat transfer in pool boiling is limited by either modifying the fluid or the heating surface. Altering heating surface geometry/topology is an easy, passive, cost-effective and robust technique to enhance heat transfer. It can be accomplished on macro, micro or nanoscale and aims at amplifying the nucleation site density, wettability or capillary wicking [34]. Surface enhancement can be categorized into three groups *i) structured surface enhancement ii) Unstructured or porous surface enhancement iii) Hybrid surface enhancement.*

2.1.1 Structured surfaces

Revising surface geometry by fabricating structured and ordered surfaces has always been an easy and favored technique to enhance heat transfer. Structured surfaces consolidate fabricating channels, fins and pins on the heater surfaces. These structured surfaces help in understanding the relationship between surface parameters (fin height, thickness, spacing, etc.) and heat transfer as these parameters can be measured and remodeled in a controllable fashion. Rise in digital technology and invention of ultra-precise, automated mechanical machining techniques enabled various researchers to design complex geometries and to study their effect on heat transfer.

Guglielmini et al. [35] first utilized the potential of macro structures by fabricating twelve copper structured surface with square pin fin cross section. They varied the height (3 and 6mm) and width (0.4-1mm) of fins, forming three different configurations of uniform and non-uniform spaced fins. Conducting pool boiling test under different saturated pressure (0.5, 1 and 2 bar) for FC-72, they observed that with increasing fin height and decreasing fin width, the HTC increases but with negligible increase in heat flux. The negligible increase in heat transfer for dense fins with increased surface area was off-set by the better wetting of boiling surface for scattered fins. On a much smaller length scale, Wei and Honda [36] tested six squared pin-fin arrays on silicon chip under subcooled FC-72 tests with altering thickness (30 and 50 μm) and height (60, 120, 200 and 270 μm), as shown in Figure 2.1. They fabricated pins using dry etch method while keeping the pin pitch, as twice that of pin thickness, constant. They observed increasing trends in HTC and heat flux values with increasing fin height and reported approximately 4.2 times increase in heat flux over that of a smooth silicon chip. The higher heat transfer efficiency was observed due to an increased wetted surface area provided by taller fins. Zhang and Lian [37] conducted experiments with pin-fin structured nickel surface with fixed 200 μm fin width, 35 μm fin height and varying the fin spacing from 200-1000 μm , as shown in Figure 2.2. They fabricated the pins using a modified lithography technique and conducted pool boiling test with de-ionized water under atmospheric condition. They conducted optimization tests for fin spacing concluding 200 μm spaced sample as the best performing configuration. The pins added surface area and their effect on vapor evolution process was a prominent factor in heat transfer enhancement.

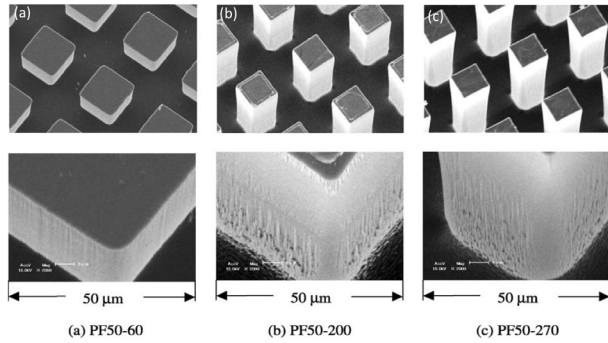


Figure 2.1: SEM images of three different micro-pin structures with increasing height. (Copyright of Wei and Honda [36]).

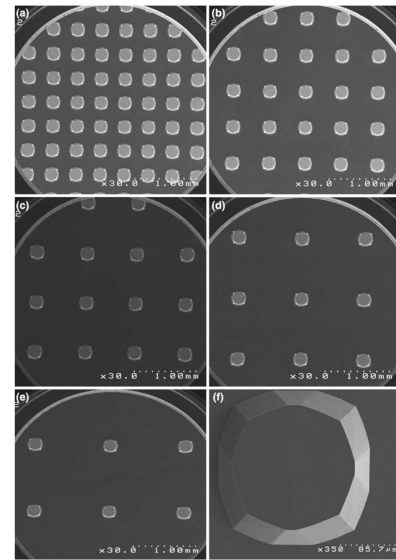


Figure 2.2: SEM images of differently spaced square pin-fins with magnified view (Copyright of Zhang & Lian [37]).

More recently, Chu et al. [38] performed extensive study on effect of micro structures on pool boiling experiments. Different micropillar configurations were fabricated on silicon substrate using etching technique by varying the height (10, 20 μm), spacing (5, 10, 15 μm) and diameter (5, 10 μm), as shown in Figure 2.3. They reported about 160% enhancement (about 208 W/cm^2) in CHF over that of plain silicon surface. Highlighting the importance of roughness augmented capillary wicking, they modified the CHF model, based on an analytical force balance approach, to include the effect of capillary wicking. On similar grounds with Chu et al., Kim et al. [39] created twelve micro-pillared surfaces with number of length scales (5-40 μm) on silicon chip samples using micro electromechanical systems (MEMS) techniques, depicted in Figure 2.4, and conducted pool boiling experiments in atmospheric conditions. They achieved about 3.5 and 3 times increase in CHF and HTC, respectively. The improvement was credited to the extended surface area and inflow of

liquid due to capillary wicking. Additionally, they developed a model to predict the capillary wicking limit to CHF while determining the optimum pin spacing as 10-20 μm . Finally, to conceptualize the effect of micro structures and the triggering mechanisms for CHF, Kim et al. [40] proposed a new model encompassing a unique mechanism which triggers CHF in micro structured surfaces. This model predicts the CHF to be triggered by the imbalance in coalesced bubble escape frequency and the liquid inflow to the triple phase contact line due to capillary wicking. They stated that the microstructures altered the thin film evaporation at the triple phase contact line, resulting in change in bubble departure frequency thus affecting CHF.

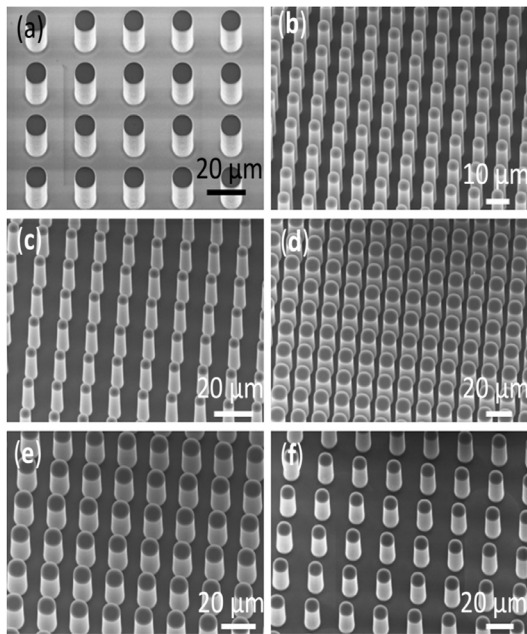


Figure 2.3: SEM images of six different configurations of silicon etched micropillars (Copyright of Chu et al. [38]).

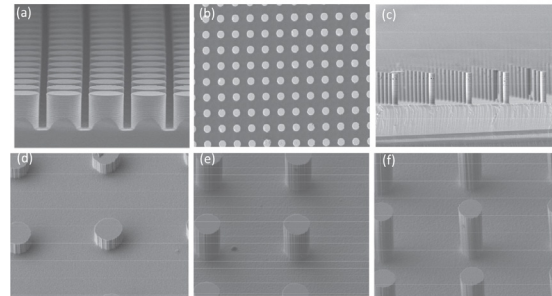


Figure 2.4: Differently spaced SEM images of micro-pin-fin silicon chip (Copyright of Kim et al. [39]).

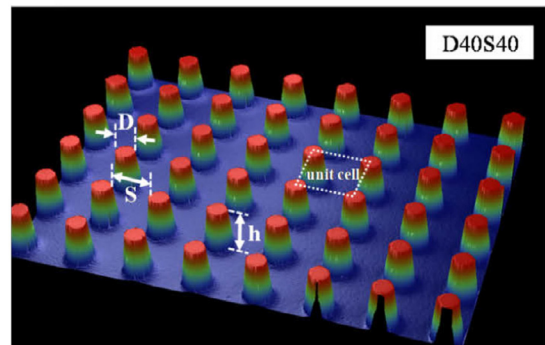


Figure 2.5: 3D profiler image of the simulated micro pillared sampled surface (Copyright of Kim et al. [40]).

2.1.2 Porous Structures

Introducing porosity is an alternative method in which a surface can be modified to enhance heat transfer. Porous surfaces are lightweight, can be easily applied to most of the surfaces, cost-effective and have a much larger impact on enhancing heat transfer efficiency as compared to solid surface. Porous structures serve three-fold purposes. First, their complex interwoven matrix has pores of multitude dimensions providing additional nucleation sites for boiling inception and growth. Second, because of their complex matrix and porosity, they assist in liquid delivery due to capillary wicking improving surface wickability. Lastly, some porous structures have pores which provide different guideways for liquid and vapor to travel thus reducing the flow resistance and enhancing flow efficiency. There are various techniques to introduce porosity onto a surface such as *i) Coating ii) Chemical treatment iii) bonding and iv) nanowires*

2.1.2.1 Coating

Forrest et al. [41] coated thin film of polymer/SiO₂ nanoparticles on 0.01 inch diameter Nickel wires and stainless steel plates with different coating thickness (300, 600, 1000 μm) fabricated using layer by layer deposition methodology. They reported up to 100% increase in HTC and CHF for pool boiling tests. They postulated that the increased surface wettability caused by the nano-porous coating along with the coatings chemical constituency affected the heat transfer process. Like Forrest et al., Feng et al [42] coated platinum nano wires (diameter = 127 μm) with alumina nano coating ranging up to 20 nm thickness. They reported a twofold enhancement in CHF owing to super wetting phenomena of alumina coating. The amorphous coating greatly enhanced the surface

wettability leading to rewetting of dry spots. Lastly, Ali and Genk [43] conducted nucleate boiling test under PF-5060 dielectric fluid with 80 μm and 197 μm thick porous copper layers coated surfaces. They studied the effect on surface inclination on these surfaces and reported approximately 5 fold increase in CHF for zero degree inclination (upward facing) orientation as compared to plain surface.

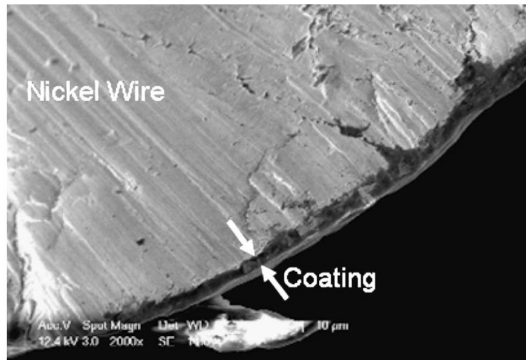


Figure 2.6: SEM image of 0.01 inch diameter nickel wire coated with 40 bilayers of polymer/SiO₂ (Copyright of Forrest et al. [41]).

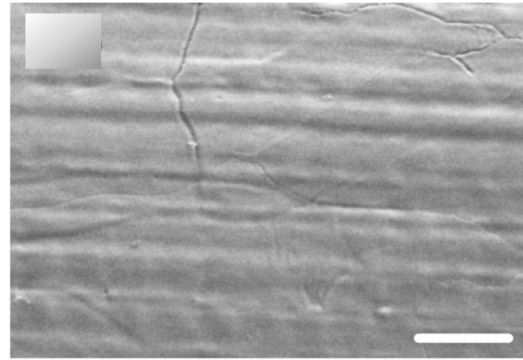


Figure 2.7: SEM images of Platinum wire with 20 nm alumina coating with scale bar as 2 μm (Copyright of Feng et al. [42]).

2.1.2.2 Chemical Treatment

Another popular porous fabricating technique is chemical treatment wherein the substrate is template with module and chemically treated to acquire a desired shape. Li et al. [44] fabricated 3D complex porous matrix structures on copper substrate using electrochemical deposition process, as represented in Figure 2.8, and conducted pool boiling experiments with R134a. Their complex, interconnected pores were a result of coalescence of hydrogen bubbles formed during electro deposition, forming natural low resistance pathways which serves as a vapor escape route during boiling aiding in heat transfer enhancement. At a heat flux of 1 W/cm^2 , they achieved about 17 times increase in heat flux compared to that of plain copper surface. Zhang et al. [45] fabricated a sponge like hybrid alumina porous structure consisting of about 100 nm smaller pore size and about 500nm larger pore size, as shown in Figure 2.9. For lower heat flux value ($20 - 40 \text{ kW/m}^2$), they obtained approximately 200% increase in HTC and about 175% increase for higher heat flux values ($40 - 100 \text{ kW/m}^2$). In this study, the added surface area and re-entrant pores offered by the interconnected, three-dimensional porous matrix demonstrated the ability of porous structures to enhance heat transfer rate. In line with Zhang et al, Ahn et al. [46] achieved a 3D foam like porous structure using reduced graphene oxide suspended in water on silicon oxide substrate. Because of the presence of porous structures, they observed a gradual increase in wall temperature at CHF as compared to rapid increase in temperature typically observed at CHF, reporting about 200% increase in CHF over that of plain surface. The amplified thermal conductivity of porous structures along with its low resistance vapor escape route proved beneficial in reinforcing heat transfer efficiency.

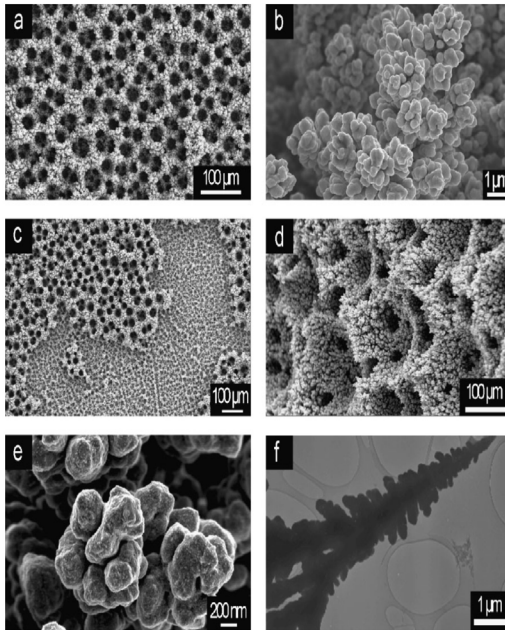


Figure 2.8: SEM images of Cu dendritic growth forming microporous surfaces with HR-SEM and TEM images (bottom two) of the Cu deposition peeled off from the surface (Copyright of Li et al. [44]).

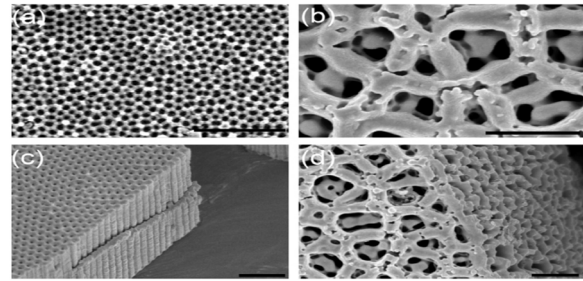


Figure 2.9: Alumina porous structure formed at two different electrolytic voltage (left) with their cross sectional view (right) (Copyright of Zhang et al. [45]).

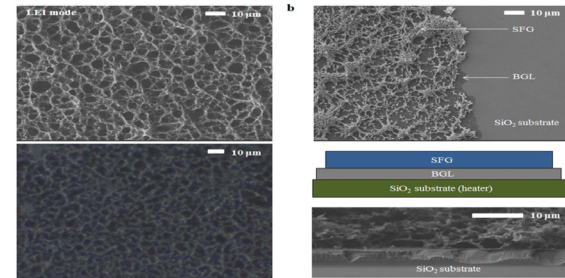


Figure 2.10: (a) SEM image of the self assembled 3D porous structure formed via reduced graphene (b) schematic representing the porous structure layering (Copyright of Ahn et al. [46]).

2.1.2.3 Sintering

Bonding pre-fabricated, porous structures with known porosity is yet another simple and cost-effective methodology to implement porous structure on a given surface. Chen and Peterson [47] sintered isotropic copper wire screens, with three different wire diameters (56, 114 and 191 μm), onto copper foil and conducted pool boiling experiments with water, under atmospheric conditions. They fabricated ten test articles to study effect of variation in porosity, pore size, coating thickness and surface condition on pool boiling. A stable, low wall superheat ($< 12^\circ\text{C}$) was observed over wide range of heat flux ($0\text{-}210 \text{ W/cm}^2$) owing to increased wetted area, nucleation sites, capillary wicking and thin film

evaporation on copper wires. Yang et al. [48] welded copper foam covers with 0.88 and 0.95 porosity onto the experimental heater surface. The copper foam had open celled dodecahedron cells with 12 to 14 pentagonal or hexagonal shapes. They conducted pool boiling tests with water and performed optimization study to report 60 ppi foam cover and 4 mm thickness as optimum value. They reported a decrease of 13K in temperature for onset of nucleate boiling and over 2-3 times increase in HTC for copper foam covered surfaces.

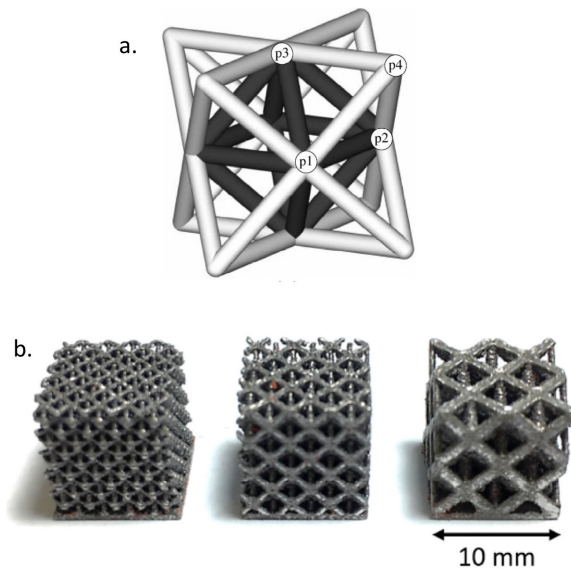


Figure 2.11: Images of unit cell representation (top) and fabricated copper foam matrices with different porosity (bottom) (Copyright of Wong & Leong [49]).

Recently, Wong and Leong [49] performed saturated pool boiling experiments for FC-72 using porous lattice structures manufactured by selective manufacturing technique. The substrates had repeated octet-truss geometry with varied unit cell size (2, 3 and 5 mm) and

height (2.5, 5 and 10 mm), as represented in Figure 2.11. Their best performing substrates, 3 mm unit cell with 5 mm height, reported 2.81 times more HTC and 5mm unit cell and 5 mm height, reported 6.11 times more CHF, as compared to a plain surface. Just like Chen and Peterson, they attributed the enhancement to increased nucleation sites and constant replenishment of liquid to the heated surface because of capillary wicking.

2.1.2.4 Nanowires

Forming porous structure on nanometer scale by growing or deposition nanowires is another practice implemented by researchers to enhance boiling heat flux. Chen et al. [50] fabricated arrays of Si and Cu nanowires by electro-less etching and electroplating technology respectively. The Si nanowires had 20-300 nm range diameters and were about 40-50 μm long whereas Cu nanowires had approximately 200 nm diameter and were 40-50 μm long, as shown in Figure 2.12. They observed two-fold enhancement in CHF and HTC attributing the enhancement to heterogeneous nucleation in between nanowires, super hydrophilicity offered by the nanowire arrays increasing surface wettability and capillary wicking. Similar to Chen, Yao et al. [51] developed a new electrochemical deposition technique to grow Cu nanowires on Si substrate with varying nanowire height (2, 5, 10 and 20 μm) while conducting pool boiling test with water as the working fluid. Their best performing sample reported almost 3 times enhancement in heat flux owing to enhanced capillary forces with added liquid delivery to hot spots.

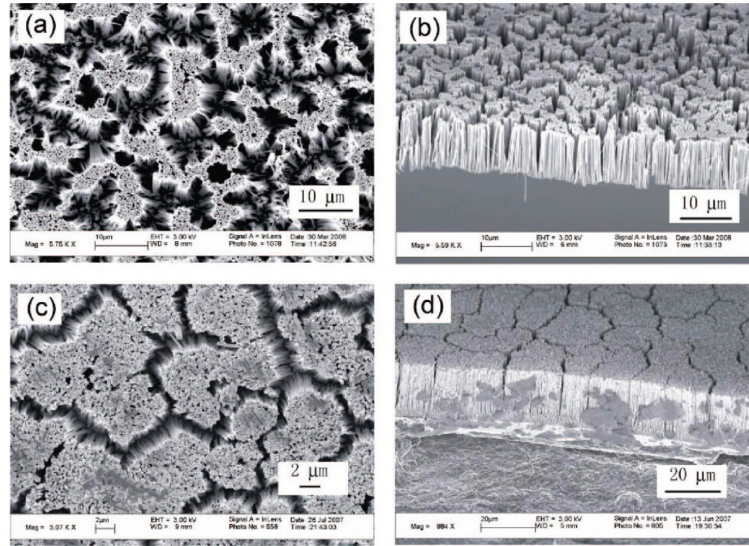


Figure 2.12: SEM images of top view (left) and cross sectional view (right) of Silicon (top) and Copper (bottom) nanowires respectively (Copyright of Chen et al. [50]).

More recently, Kumar et al. [52] electrodeposited Cu and Ag nanowires with alumina-based template methodology with template having diameter of 200 nm and different inter-pore distance (260, 320 and 360 nm). They conducted pool boiling experiments using FC-72 as working fluid. The improved surface nucleation density offered added surface area and liquid replenishment resulted into increased HTC, heat flux in addition to decrease in the boiling inception temperature.

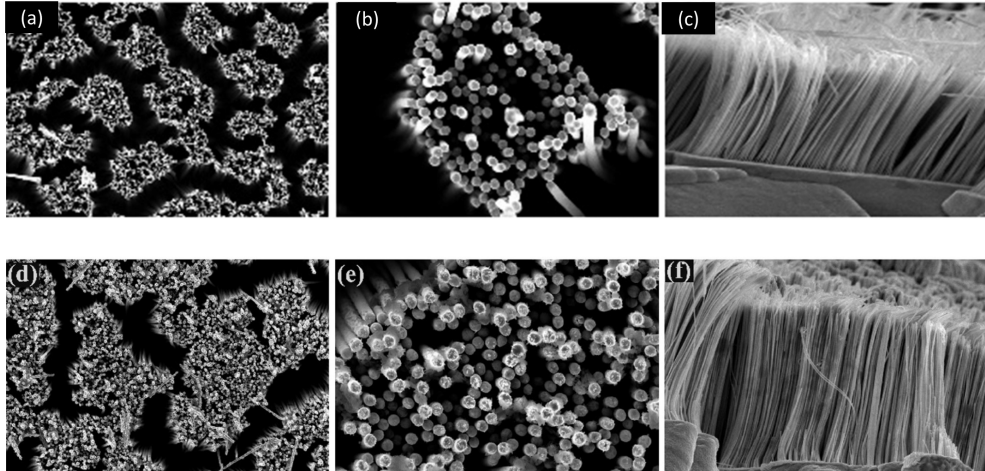


Figure 2.13: FESEM images of nanowires indicating top view, diameter and height (left to right) for Copper (top) and Silver (bottom) respectively (Copyright of Kumar et al. [52]).

2.1.3 Hybrid Structures

Researchers long realized the potential of combining surface features to further enhance the overall heat transfer process. With the added benefits of the surface modifications being combined, these hybrid structures proved highly effective in enhancing heat transfer. Depending upon the combination of surface enhancement strategies, there are two common structure that are fabricated *i) Modulated structure (Porous + micro-structures)* *ii) Hierarchical structure (micro-structures + nanowires)*.

2.1.3.1 Modulated Structures

Deng et al. [53] fabricated porous structures with reentrant cavities microstructure surfaces using copper powder (50-75 μm sized) via sintering method, as shown in Figure 2.14(I). They conducted subcooled (3-30 $^{\circ}\text{C}$) pool boiling experiments with water and ethanol. They observed significant reduction in ONB and about 3, 5.3 times enhancement in HTC with water and ethanol, respectively. The enlarged surface area offering additional

nucleation sites along with improvement in liquid replenishment yielded the amplified boiling characteristics. Liter and Kaviany [54] fabricated modulated porous coating of copper for enhancing pool boiling heat transfer. They deposited a layer of copper powder (200 μm sized spherical particles) with periodically, non-uniform thickness representing inverted cone like porous structures, depicted in Figure 2.14(II). This design was intended to create separated liquid vapor pathways with the porous structures providing preferential liquid suction like thermosiphons. They reported a substantial decrease in ONB with 3 times increase in CHF as compared to plain surface. Similar to Liter and Kaviany, Li et al. [55] fabricated modulated hybrid porous structures varying the base and pillar particles size and conducted pool boiling experiments with deionized water. Their best performing sample was base and pillar consisting of 250 μm sized particles, reporting 3 times increase in CHF and HTC over plain surface.

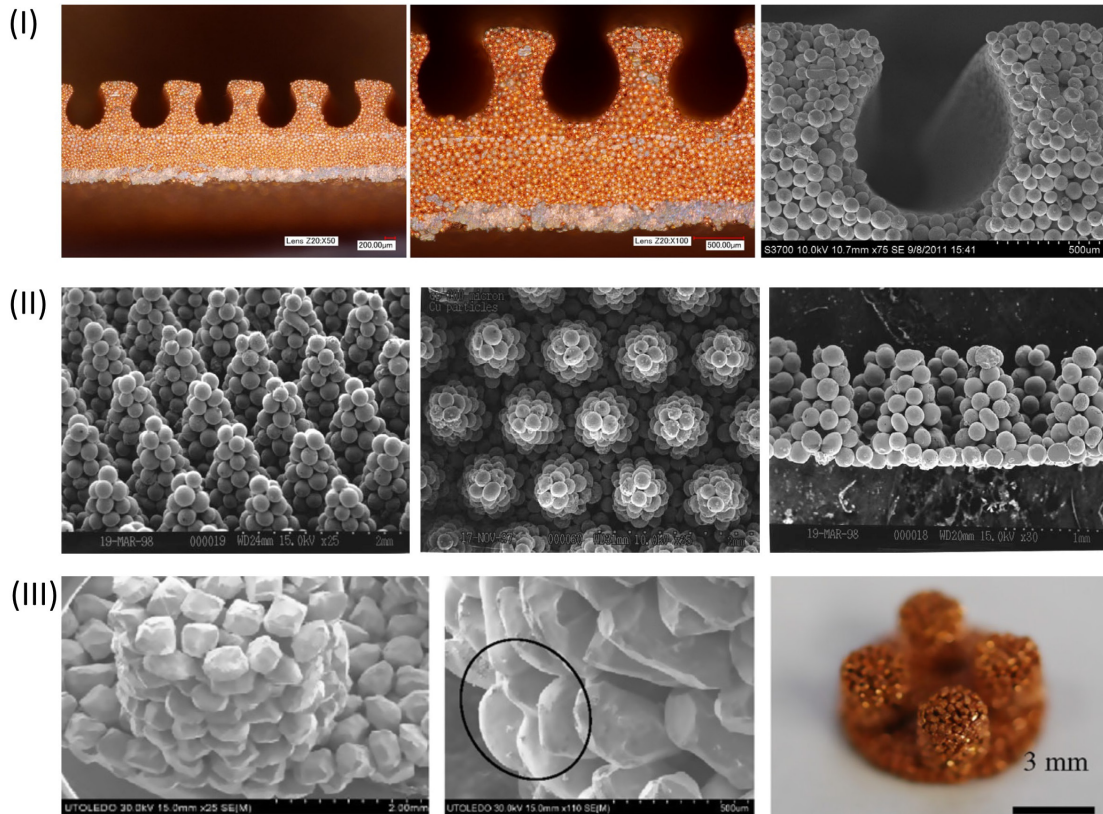


Figure 2.14: SEM images of modulated hybrid structures by three different research groups. (I) Geometric representation of porous structures with re-entrant cavities at three different magnification from left to right (Copyright of Deng et al. [53]). (II) SEM images of porous modulated structures fabricated from spherical copper particles indicating side view, top view and perspective view from left to right respectively (Copyright of Liter and Kaviany [54]). (III) SEM images of modulated porous structures of 500 μm thickness and 250 μm particle size (Copyright of Li et al.[55]).

2.1.3.2 Hierarchical structure

Chu et al. [56] in advancement to their previous work [38], deposited silica nanoparticles and copper oxide on silicon and copper micro-structured surfaces, respectively, as shown in Figure 2.15. They conducted pool boiling with different roughness factor to study the importance of roughness on overall heat transfer process. They argued that the increased roughness amplified the surfaces capillary forces which aids in delaying CHF and achieved about 200% increase in CHF as compared to plain surface. On similar grounds with Chu,

Rahman [57] bio templated Tobacco Mosaic Virus on silicon micro structures creating super hydrophilic surfaces, shown in Figure 2.16. These viruses greatly influenced the surface morphologies, creating nanowires on them, inducing additional wickability. This further stressed the important role of wickability on overall heat transfer process. They reported about two times increase in CHF with water as fluid in pool boiling tests. Lastly, Dhillon et al. [58] conducted studies with different surface nano-textured, micro pillared surface to study and develop a thermal- hydraulic coupled CHF model. They grew nanograss on Si chip and observed that the CHF can be enhanced via microstructure facilitated liquid transport to the hot dry spot. They observed an optimum gravity driven capillary wicking spacing between pillars as 200 μm stating that with further decrease in spacing, to 10-20 μm , viscous pressure dominates capillary wicking ceasing additional CHF enhancement.

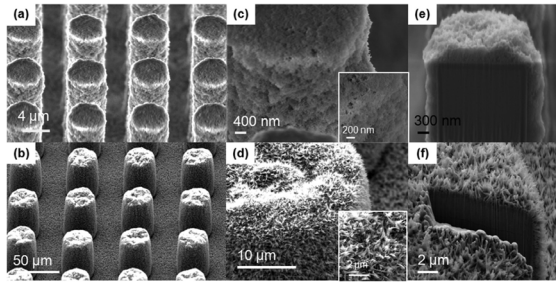


Figure 2.15: SEM images of Silicon (top) and Copper oxide (bottom) based hierarchical surfaces with magnified view from left to right (Copyright of Chu et al.[56]).

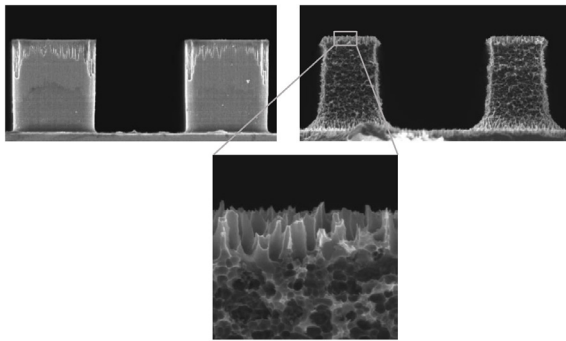


Figure 2.17: SEM images of (a) micro textured surface with plain square micropillar (b) nano textured micropillar covered with nanograss (Copyright of Dhillon et al. [58]).

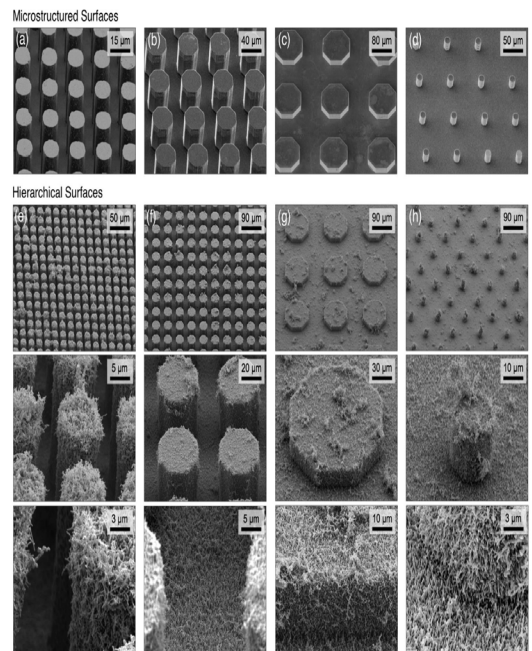


Figure 2.16: SEM images of the four different microstructure samples (left to right) with hierarchical surfaces grown on them. Each columns indicating three different magnifications levels (Copyright of Rahman et al. [57]).

3 Objective and Concept of this research

Majority of modern heat transfer systems rely on boiling phenomena for very large heat flux removal capability. These systems operate in nucleate boiling regime which is limited by CHF. There is an ever increasing demand for enhanced phase-change heat transfer rate, via passive strategies, to further exploit the advantages of boiling. Delaying CHF expands the amplitude of heat of a given boiling systems, and thus broadening its application range. Also enhancing HTC is highly desirable because large amount of heat can be extracted without much rise in surface temperature.

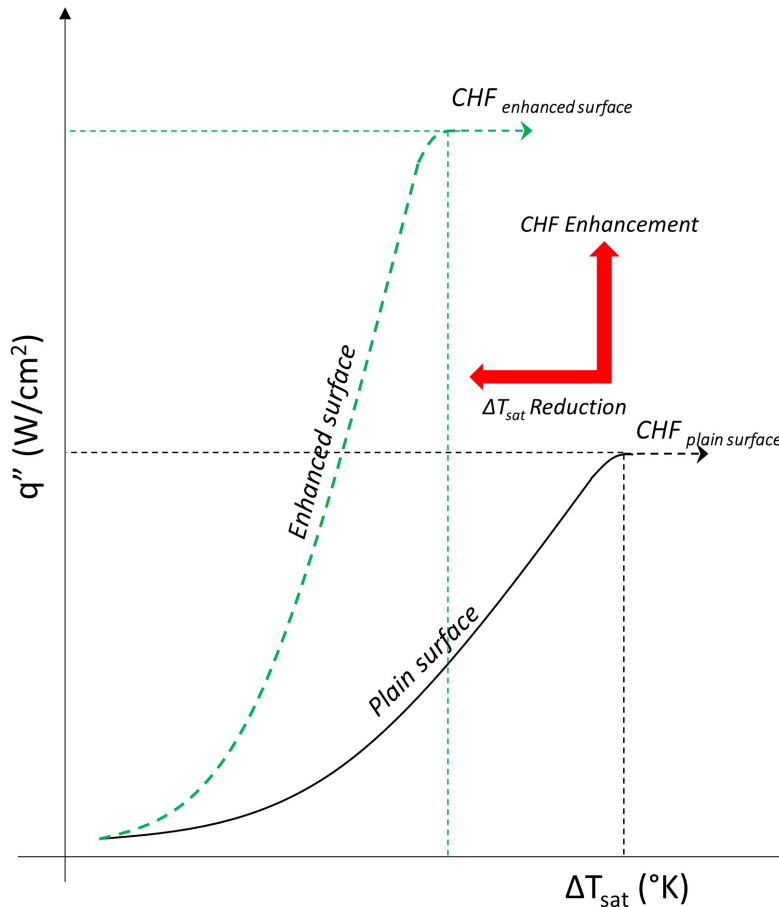


Figure 3.1: Graph indicating the objective of the research to enhance CHF while simultaneously reducing the excess temperature.

Delaying CHF while increasing the heat transfer coefficient can be ensured via introducing surfaces modifications on the heater surface, as shown in Figure 3.1. Surface modifications alters active nucleation site density, wetted surface area, surface roughness, wettability and wickability. These are some of very critical parameters which highly affects the heat transfer and have been extensively studied by researchers over past decades. Lately, the importance of combining these surface enhancements has seen great exposure by researchers worldwide.

Research done till date have been to enhance and optimize wickability in a plane which is parallel to the heater surface. This in-plane wickability is greatly hampered once we reach closer to the CHF. At CHF, a vapor cushion covers the heater surface, there is minimal in plane wickability and the heat transfer is thus greatly affected because of lack of liquid for heat transfer. With this study, we are advancing the current research exploration in wickability by introducing a novel matrix structure which offers out of plane capillary wicking capability, in addition to in plane wickability. The interwoven matrix structure introduced offers preferential pathways in a direction perpendicular to heater surface. These preferential pathways offer out-of-plane capillary wicking, in addition to in plane wickability. Out of plane capillary wicking is vital during CHF as it offers additional liquid supplement for further enhanced thin film evaporation. The first objective of the study is to explore the effect of this out-of-plane capillary length scale on overall heat transfer performance.

Secondly, to further optimize the out of plane capillary wicking, we focus on decoupling the viscous drag losses from the capillary wicking pressure by growing nanowires on them.

The chemical treatment utilized to introduce nanowires changes the wettability and roughness of the surface. The nanowires provide the enhancement in generating the capillary pressure as well as the preferential pathways of the matrix offers low viscous drag resistance pathways for liquid supply. This decoupling of the capillary pressure from the viscous drag losses is a major contributor is optimizing the in/out of plane capillary wicking.

In this study, we attempt to combine microstructure porous surface enhancement methodologies to test and understand their combined effect on overall heat transfer process. Here we introduce a novel, 3D porous, pillared, micro-structure surfaces to enhance the rate of heat transfer. The 3D porous pillars forms intended guideways to the heater surface. These guideways offer preferential, out-of-plane liquid supplement to the heater surface. This is done by introducing augmented roughness, facilitating continuous supply of liquid to the heater surface by in/out of plane capillary wicking and decoupling the liquid and vapor pathways. These are further elaborated in the subsequent discussions.

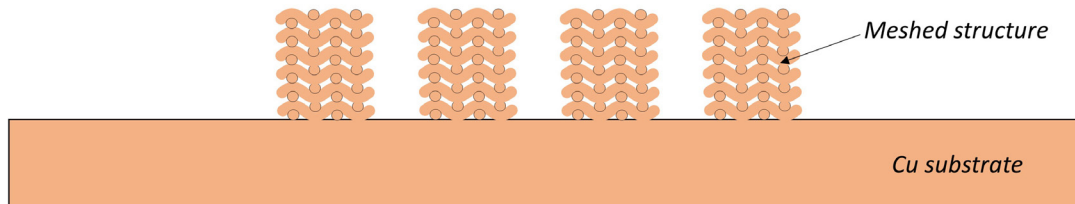


Figure 3.2: Test sample surface geometry schematic of the designed surface topology

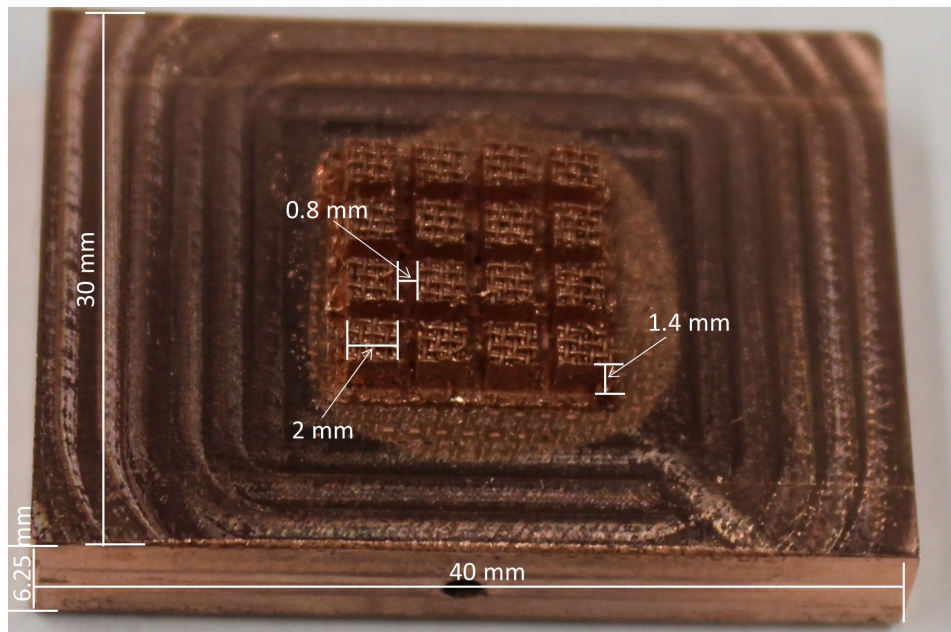


Figure 3.3: Test sample surface geometry Image of the actual fabricated test sample with dimensions

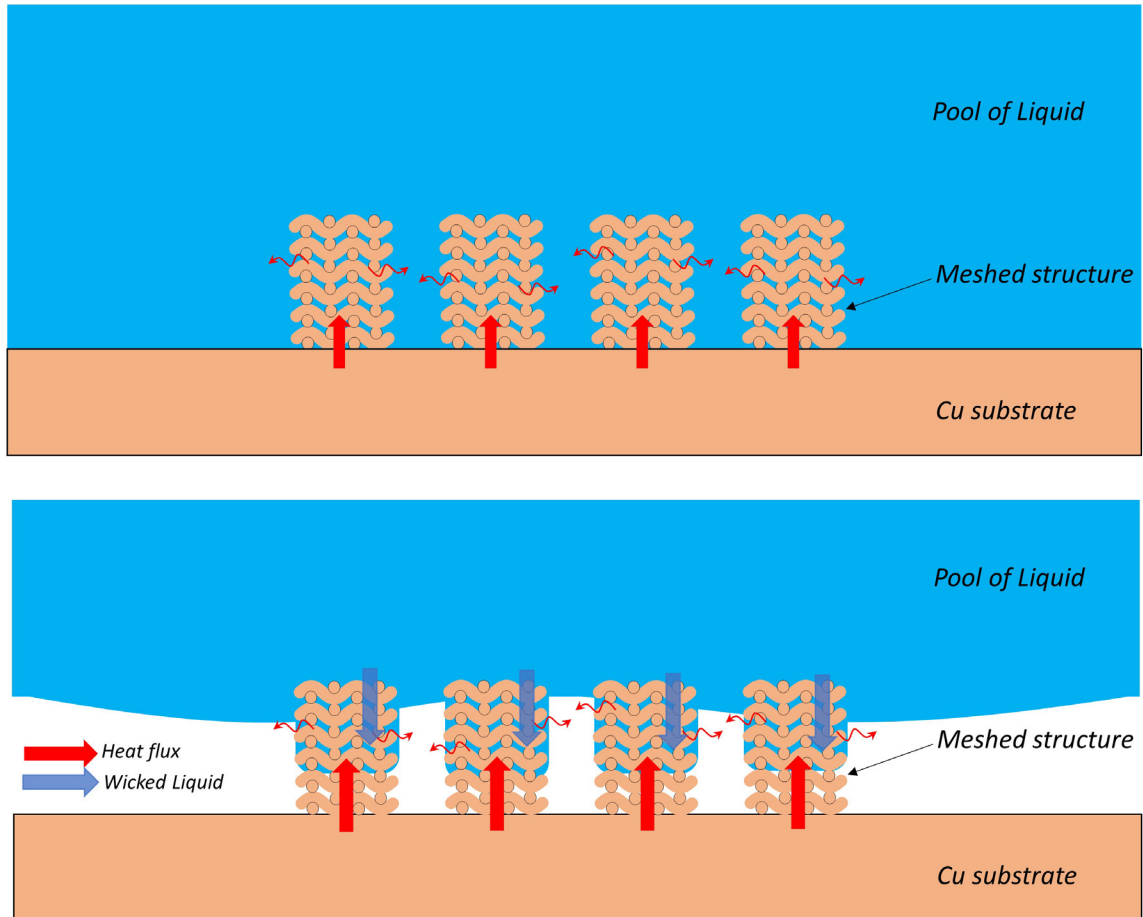


Figure 3.4: Schematic representation of top: sample under test before CHF and bottom: sample under test during CHF.

3.1 Augmented Roughness

The effect of augmented roughness on heat transfer can be better described by its three characteristics: increased nucleation site density, increased wetted area and elongated contact line. Roughness introduced by micro/nano, gaps of the proposed porous structures introduces additional cavities, increasing nucleation sites, and thus further initiating boiling at these locations. Also, to have cavities activated and thus contributing to overall heat transfer, the size of these cavities should correspond to the critical cavity size for the desired wall superheat region. Additionally, these structures enlarge the wetted surface area, and

thus expanding the solid-liquid contact. Lastly, as introduced in the heat transfer model, heat transfer is dominated by thin film evaporation occurring at the solid-liquid-vapor contact line. Stretching the contact line amplifies the thin film evaporation mode of heat transfer, and thereby augmenting heat transfer.

The cavities formed by proposed porous structures and nanowires grown on them correspond to the critical radii of surface cavities for the desired wall superheat (10 – 20 °C). The wire mesh provides additional surface area along its periphery for added liquid-solid contact. Also, the wire are woven in such a way that the porosity introduced induces wicking as well as thin film evaporation.

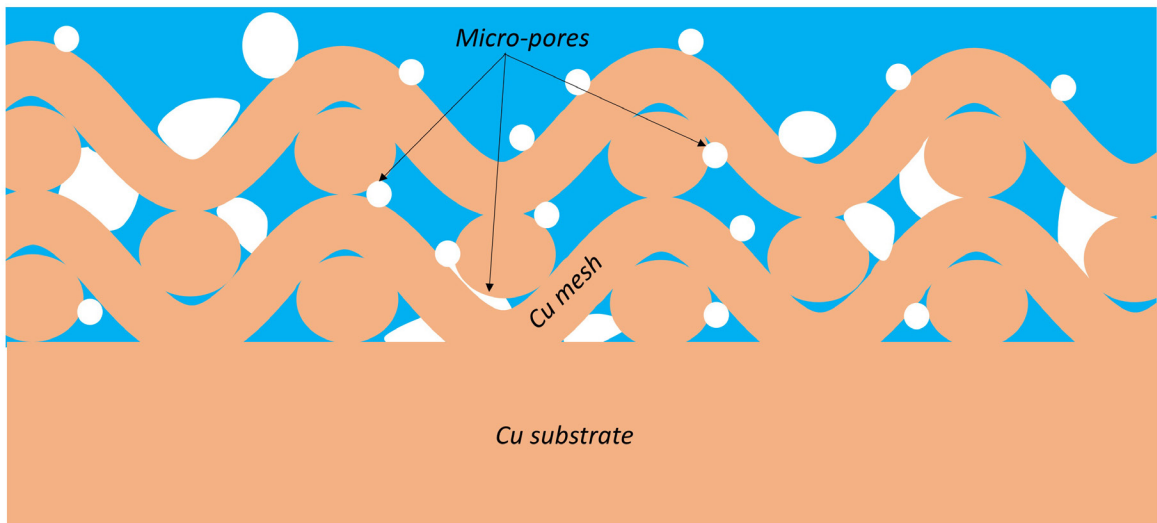


Figure 3.5: Schematic indicating additional nucleation because of formation of micro-pores due to meshed structures

3.2 Promoted liquid supply

Surface wettability and wickability is crucial in ensuring adequate supply is facilitated to the heater surface. Improving surface wettability reduces the drag force along the liquid

flow path to the heated region or dry spot. Wettability can be substantially improved by making the surface super hydrophilic. Hydrophilicity can be introduced by micro/ nano structured, porous surfaces or hierarchical surfaces. Wickability is the capillary pumping force which induces micro inflows to the heater surface. The narrow gaps introduced by microstructure spacing or pore size generate micro inflows. The micro inflow is the force due to intermolecular forces between the liquid and the surrounding solid spacing and is a balance between the capillary pressure force and viscous losses.

The pillar spacing in our study ensures macro in plane wicking of liquid to the heater surface. The porosity introduced by layering mesh over each other ensures the out of plane capillary wicking of liquid to the heater surface. This out of plane wicking contrasts with the macro pillar induced, in-plane wicking and provides additional assistance in promoting liquid to the heater surface. Also, with this additional liquid supply, CHF can be further delayed as well.

3.3 Decoupled liquid/vapor pathways

CHF is the formation of a vapor layer when the resistance for bubble motion inhibits bubble escape. To enhance CHF, the bubble motion dynamic can be altered by providing separate pathways for liquid and vapor flows. For pool boiling process on a plain surface, evaporation pulls the liquid-vapor interface and the bubble expands in all direction due to symmetry. As shown in Figure 3.6 , in case of channels and fins, a bubble grows on the edge of channel or fin. However, due to absence of one of the momentum force components, the bubble is targeted away from the heater surface. This motion of bubble

induces bulk liquid motion over the channel or fin, and thus separating the liquid vapor pathways.

The pillar-structured surface, in this study, is introduced with the idea of separating the liquid, and vapor pathways, reducing vapor escape resistances, inducing adequate liquid supply to the heater surface and delaying CHF.

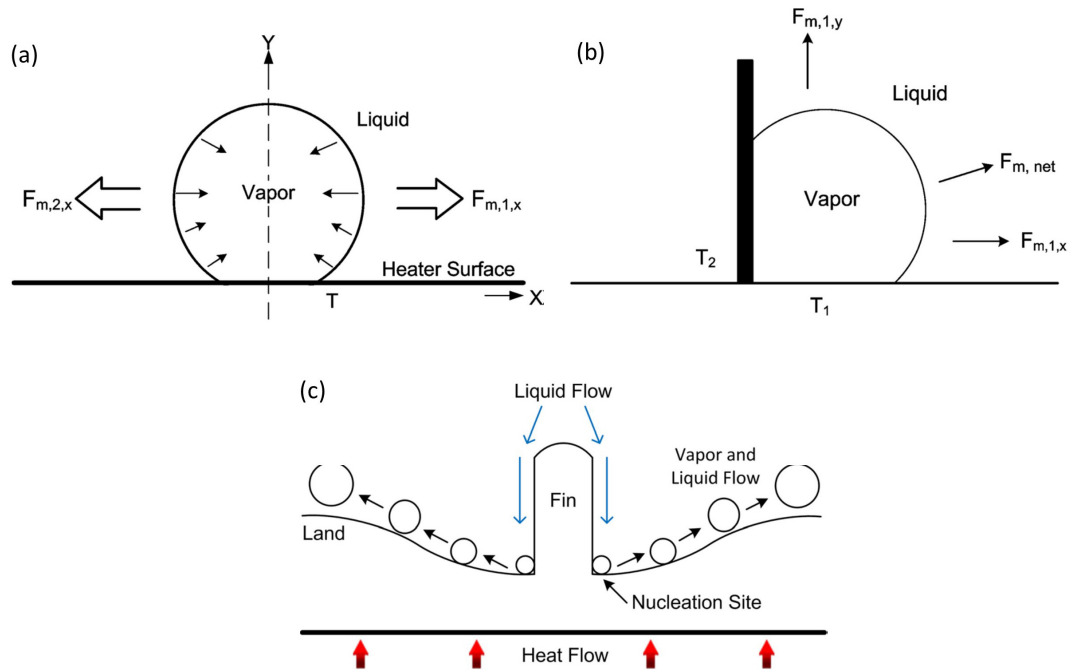


Figure 3.6: Schematic showing the momentum forces acting on bubble on (a) plain surface (b) corner of channel and (c) flow of liquid across a fin (Copyright of Kandlikar et al. [59])

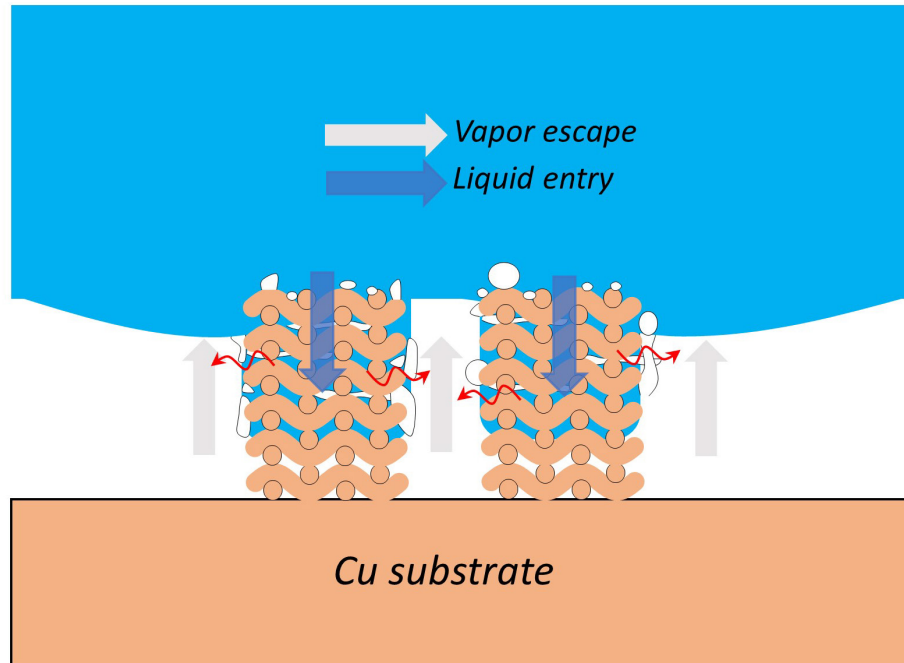


Figure 3.7: Schematic representation liquid pathway through the mesh while vapor escaping from the sides of the meshed structures.

4 Fabrication

4.1 Fabrication of test samples

4.1.1 Diffusion bonding

Diffusion bonding is a direct metal to metal, joining process which happens at the solid-solid interface. It usually occurs at very high temperature and high pressure force [60].

Diffusion bonding takes place in three stages [60].

1. At high temperature and pressure force, defects present on the two meeting surfaces plastically deform, interlink with one another and form an interface
2. Elevated temperature and pressure lead to creep and change of grain boundaries forming isolated pores. At elevated temperature, exchange of electrons and bond. Describe diffusion bonding.
3. Lastly, molecules of the two metals diffuse across the interface, mixing and forming a bond.

Diffusion bonding performed for this study is done under vacuum to avoid any impurity contamination and oxidation on the surfaces at elevated temperature.

The wicking structure were fabricated using high vacuum, high temperature diffusion bonding process. The substrate onto which the copper meshes are diffused was cut from a quarter inch copper bar into 30 mm × 40 mm × 6.25mm in size (length × width × thickness). A hole of 1.5mm was drilled at the center of the substrate to a depth of 15 mm. This hole was drilled to insert a k-type thermocouple for measuring temperature. The substrate was polished using 1000 grade sand paper to prepare a smooth surface to facilitate diffusion.

After polishing, the surface was cleaned with acetone wipe and blown dry to produce a highly smooth surface to facilitate proper diffusion. The copper mesh was cut into 20 mm × 20 mm pieces and was cleaned under DI water, IPA, acetone and was blown dry using dry compressed air.

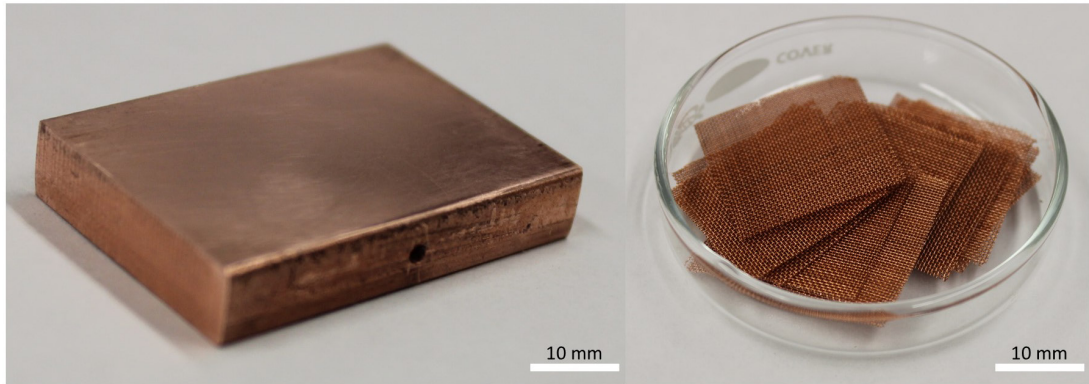


Figure 4.1: Image showing the copper substrate and the copper meshed after cleaning them, ready for diffusion bonding

A custom-made diffusion bonding setup was designed and used to facilitate high temperature and high clamping force necessary for effective diffusion bonding. After several trial and error, a robust, reliable operating parameters was deduced which produced consistent and strong diffusion bonding sample.

Table 4.1: Specification of the inter-woven copper meshed onto the substrate

Sample	H ₁	H ₂
Opening (mm)	0.2794	0.2794
Wire diameter (mm)	0.2286	0.2286
Number of Layers	6	12
Total Mesh Thickness (before bonding)	2.91 mm	5.82 mm
Total Mesh Thickness (after bonding)	1.4 mm	2.6 mm

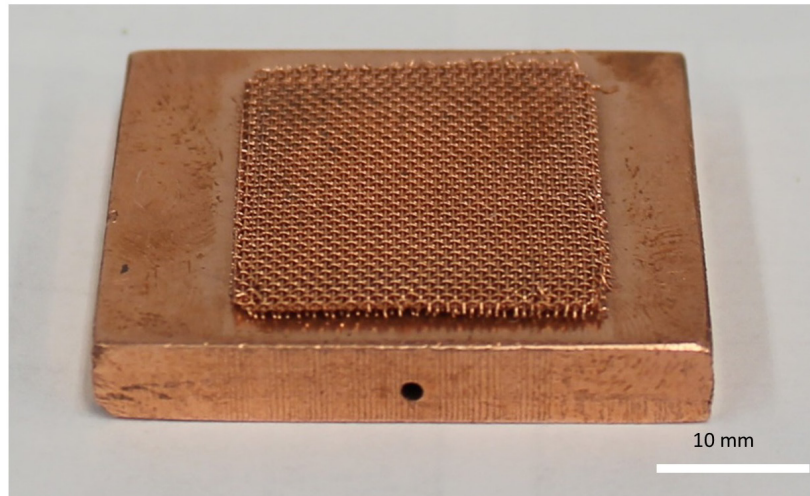


Figure 4.2: Sample after diffusion bonding

4.1.2 Machining of Test samples

The bonded sample is removed from the bonding setup and cleaned with water, acetone and blown dry with air. The total height of the diffused copper mesh is measured. To further incorporate pillars into the wicking structure, the sample was machined with high precision CNC machining process. Depending upon the height of the pillars, a 3D CAD model was prepared in Solidworks which was then used to produce a G-code in NX Unigraphics to automate the CNC process. CNC milling was necessary as the feed rate, depth of cut must

be precise to avoid any damage or de-bonding of the surface. As the spacing between the pillars was 800 μm , the tool used for the machining was a 1/32th inch ($\sim 793 \mu\text{m}$) with a feed rate of 0.5 ipm and at 2000 rpm. The final fabricated porous, pillar-structured samples is shown below in Figure 4.3.

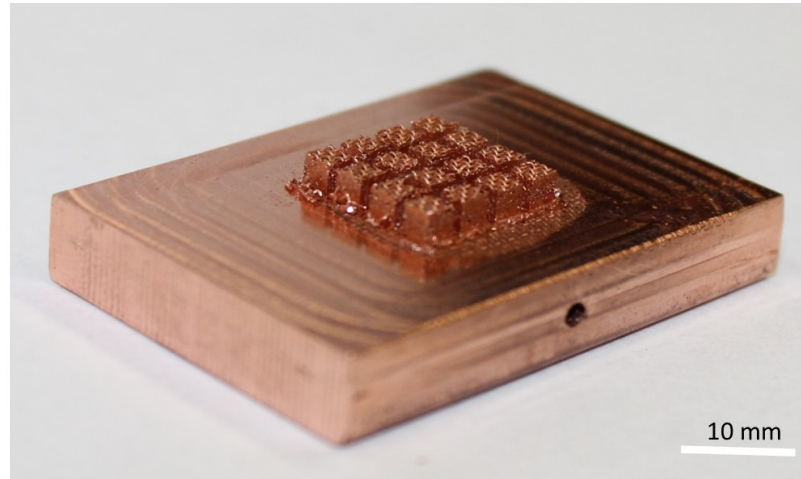


Figure 4.3: Final machined test sample

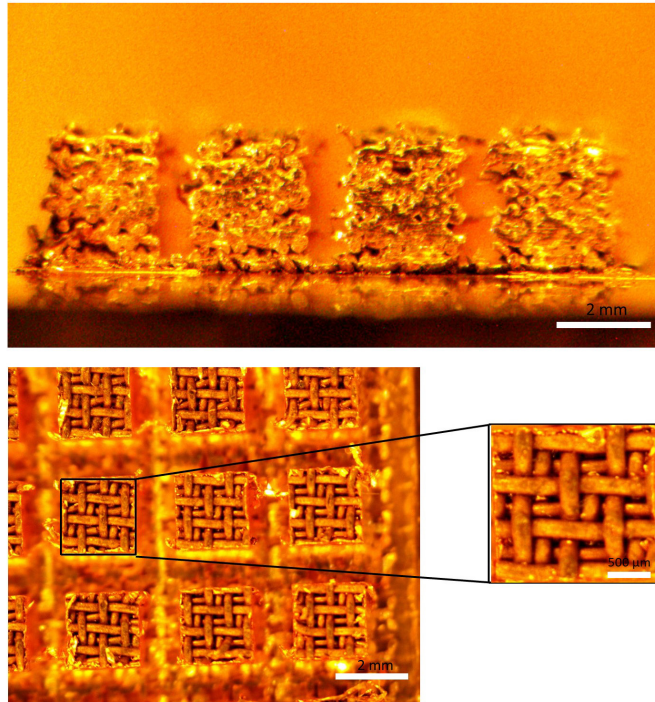


Figure 4.4: Microscopic images of the test sample with top: cross sectional view and bottom: plan view with enlarged pillar image

4.1.3 Acid Cleaning

To remove any contamination/impurities and any oxide build up, an acid cleanup was done on the surface using 15% by weight nitric acid solution. The sample was placed in the acid solution with a stirrer for 20 minutes and then was rinsed with DI water and blown dry with air.

4.1.4 Nanowire growth

Based on the chemical treatment procedure prescribed by Huang et al. [61], the following procedure was undertaken to successfully grow nanowires on the copper meshes.

4.1.4.1 Acid Washing

To facilitate the growth of copper oxide nanowires on the mesh wire, it was necessary to free the wire from nascent oxide layer naturally present on the wires. To do so, sample was acid cleaned. The sample was immersed in 30% by weight nitric acid solution and was stirred for about 15 minutes. The sample was removed from the solution and repeatedly cleaned with DI water and blown dry with compressed air to remove any acid solution left in the pores. Finally, the sample was kept on a hot plate at 60°C for 10 minutes to evaporate excess water in it.

4.1.4.2 Chemical Treatment.

The next step after acid cleaning was to insert the sample into 30% by weight hydrogen peroxide solution for another 40 minutes. The sample was constantly stirred to ensure proper mixing after which it was removed and cleaned with DI water and blown dry with air. It was finally placed on the hot plate at 60°C for 10 minutes for complete drying.

The appearance and the color of the copper changed which indicated the growth of nanowires. A water droplet was placed on the copper mesh to see the effect of copper nanowires on contact angle and wettability. The water droplet immediately was wicked inside the pores. When the droplet was placed on the copper substrate, it showed almost 0° contact angle indicating the change of surface to superhydrophilic.

SEM images, as shown in Figure 4.5, depicts the formation of copper nanowires on the surface of the interwoven copper mesh. Cracks appearing on the surface can be attributed

to the thermal stresses developing on the curvature of wire leading to rupture of the surface, forming micro cavities.

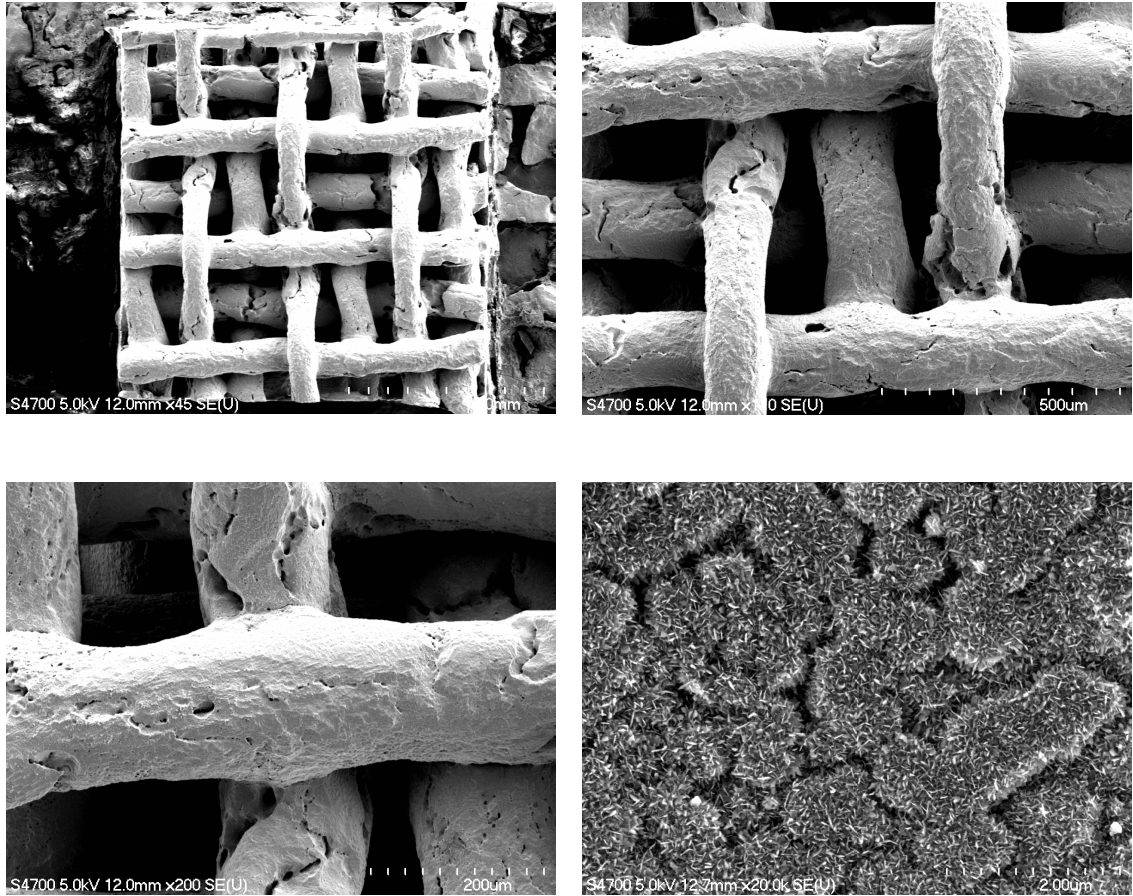


Figure 4.5: SEM images of the micro-structured pillar at different magnification level.

4.2 Fabrication of the experimental setup

4.2.1 Heating block and 1D column

The heat flux into the sample was transferred using a heat exchanger designed to support 1D heat flux to the porous samples. The heat exchanger consists of a heating block and a

1D column. The heating block was machined out of a stock copper block to required dimensions of width 45 mm, length 50 mm and height 25mm. Three holes, 7/16 inch (11.12mm) in diameter were drilled into the heating block for provision to accommodate cartridge heater. The cartridge heater was used as a heating source which would provide the necessary heat energy to generate heat flux. Two cartridge heaters (9.5 mm, 50mm length) was used which provided 400W of power for heating.

The 1D column was 25 mm long with 10 mm × 10 mm cross sectional area. Three holes of 2.4 mm in diameter and 5 mm deep were drilled at 10 mm equidistant apart from each other. Since the length and width of 1D column is comparably smaller than its height, later heat transfer was negligible, and heat was conducted only along the height of the 1D column. K-type thermocouples were inserted into the equidistant holes for real time heat flux measurement. By measuring the temperature difference between these thermocouples, the heat flux to the sample can be easily calculated. The 1D column was then brazed to the heating block orthogonally and the final assembly is as shown in Figure 4.6.

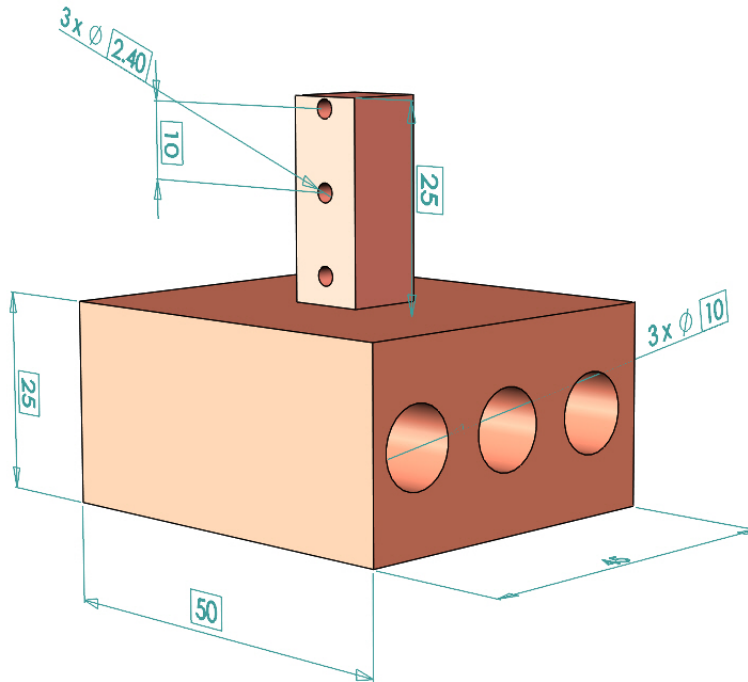


Figure 4.6: 3D CAD model representing the heating block with 1D column.

4.2.2 Acrylic Tube and O rings

To bind the pool of liquid on to the sample surface and to promote visualization, transparent acrylic tube (HYGARD ®) of 44.45 mm diameter, about 3 mm thickness and 150 mm in length was used. To prevent any leakages from the ends of the tube, two O-rings (44 mm diameter) were inserted into the slots in the mounting plate. The ends of the tube were pressed against the O-ring to have a leak proof system.

4.2.3 Mounting Plates

The mounting plates, top and bottom, as show in Figure 4.7 and Figure 4.8, were designed to fit the acrylic tube, heat exchanger and the steel pipe. The top plate was made of cooper with 60 mm × 60 mm × 6.35 mm width, length and thickness respectively. The top plate had provisions for inlet/outlet pipe for heat exchanger and steel pipe with holes drilled. The

heat exchanger and the steel pipe were inserted into the provisions provided in the top plate and was brazed to their respective positions.

The bottom plate had a slot of 11 mm × 11 mm to expose the desire mesh area to a pool of liquid. Surrounding the 11 mm × 11 mm slot, trenches were drilled to accommodate the acrylic tube and an O-ring. Holes of 6.4 mm were drilled to assemble the entire experimental setup and secure the test setup onto the test bench. A bottom mounting plate was used to secure the entire setup to the table via sandwich the test sample in between the heating block and the test setup as shown in the Figure 4.11. A silicone rubber (1.5mm thick) with a slot of 11 mm x 11mm, was used which served dual purpose. Firstly, it insulated the sample and prevented any heat flux to be transferred from the non-meshed area of the sample. Secondly, it prevented any leakages from the sample and mounting plate interface.

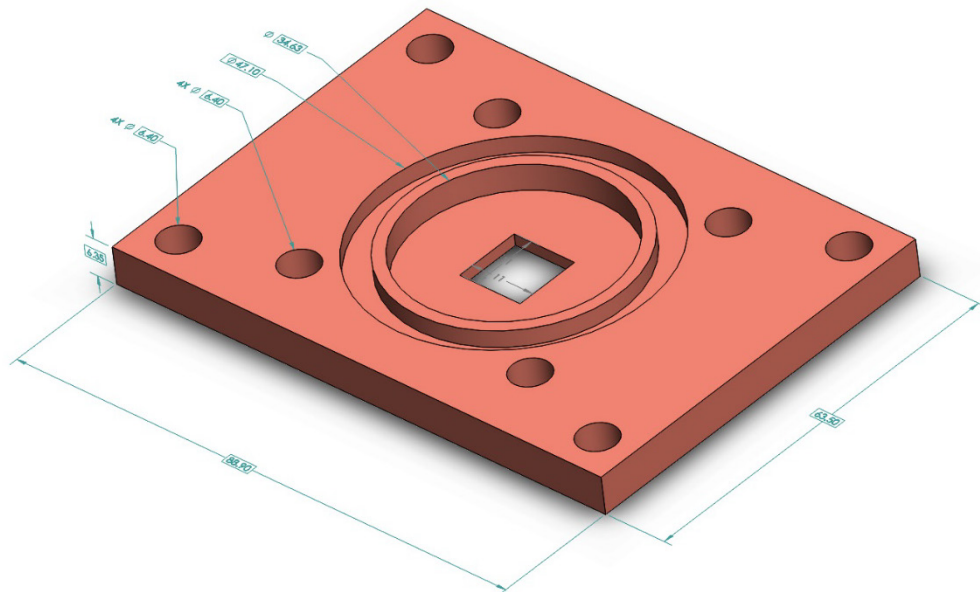


Figure 4.7: 3D CAD model of Bottom mounting plate.

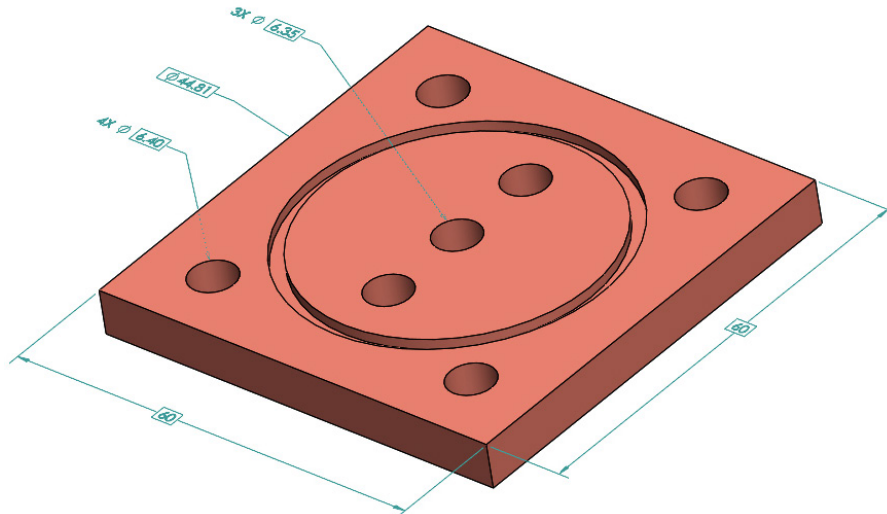


Figure 4.8: 3D CAD model of Top mounting plate.

4.2.4 Condenser, chiller and rope heaters

The condenser used to condense the evaporated water back to the pool of liquid was made of copper tubing and designed into helical shape. The design and the number of turns were estimated from the energy balance into the experimental setup. Cold water at around 25°C, from the chiller, was constantly flowing through the coil to ensure efficient condensation. To assure that the pool of liquid is maintained close to the saturation temperature, auxiliary rope heaters (136 W/m, 4.31 mm thickness, 1m in length,) were wound around the acrylic tube and heated to provide auxiliary heating.

4.2.5 Electrical devices

The power to the cartridge heater was transferred from the high voltage variac and multimeter were attached to it to measure the current and voltage supplied. The cartridge heaters were connected in series. Agilent data logger was used to measure and log the temperature value and to see the whether the setup has reached a steady state or not.



Figure 4.9: Power source for cartridge heater, VARIAC



Figure 4.10: Agilent DAQ system

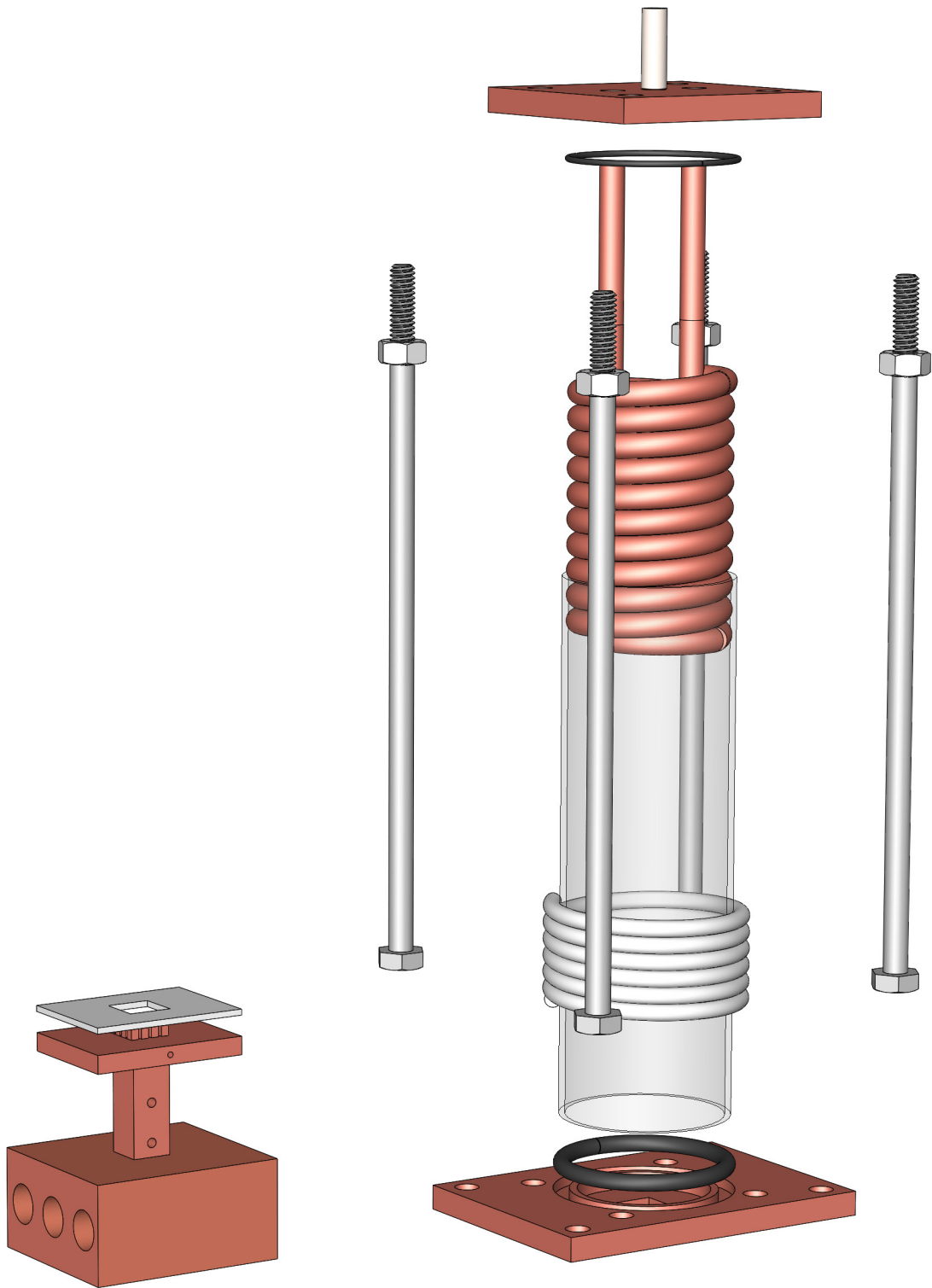


Figure 4.11: Exploded view of the final assembled 3D CAD model of the experimental test setup.

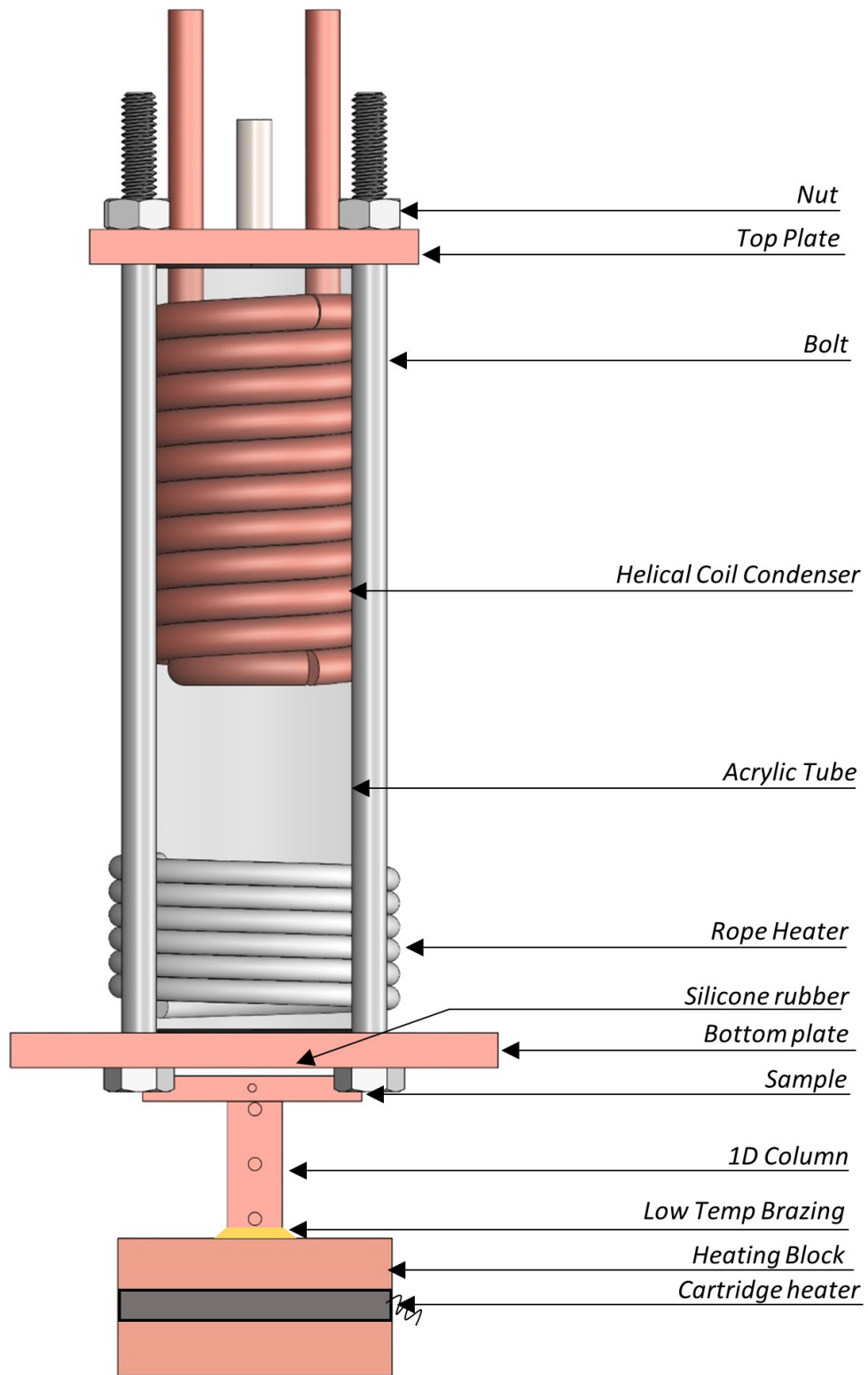


Figure 4.12: Schematic of Test setup with different sub components.

5 Experimental setup and data analysis

5.1 Experimental procedure

The objective of the research was to see the trend/nature of heat flux against the excess temperature in addition to finding the critical heat flux values for the samples under consideration. A constant heat flux in steps was supplied to the experimental setup and the pool boiling graph is then plotted for evaluation. Test sample was placed onto the heating column and a thermal epoxy was used in between to reduce any contact resistance. Also, to prevent any heat loss from the experimental setup and to ensure 1D heat flux criteria, the heat block assembly, 1D column and samples were insulated using mineral wool. The testing protocol is described below.

- Mount the test sample onto the 1D column and assemble it as shown in the Figure 4.12.
- Insert the thermocouples into their respective holes in 1D column and in the sample. Insulate the heating block, 1D column and the sample using mineral wool.
- Fill in the acrylic tube with measure 50 milliliter quantity of DI water.
- Make all the electrical and electronic connections to the variac, multimeter and the data logger. Switch on the auxiliary heater to degas the liquid pool.
- Turn on the main supply from variac and start initial heating.
- Wait for steady state to be condition and record the temperature readings. Calculate the heat flux and the excess temperature while simultaneously plotting the boiling curve.

- Increase the supply voltage. Repeat the process until the system reaches closer to the CHF.
- When the system is closer to the CHF, reduce the step voltage and constantly monitor the temperature.
- When the surface temperature overshoot, it indicates CHF has been reached. Immediately cut off the supply power from the variac and insert cold water into the system to bring down the temperature.

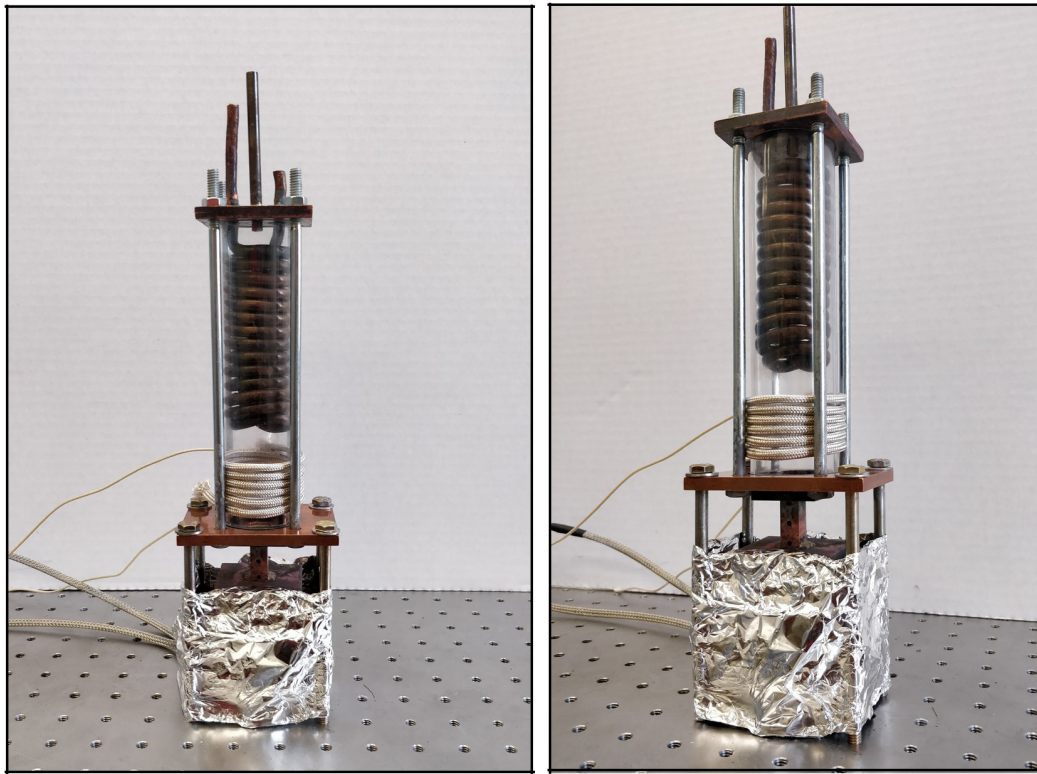


Figure 5.1: Image of the assembled test setup.

5.2 Data Analysis

The heat flux, surface temperature and heat transfer coefficient are interpolated using the four thermocouple data from the 1D column and sample holes, as shown in Figure 5.2.

The 1D column assumes a linear heat flux transfer towards the sample. Accordingly, by Fourier 1st law of 1D conduction, the heat flux through 1D column into the sample is given by Equation (4) , as shown below

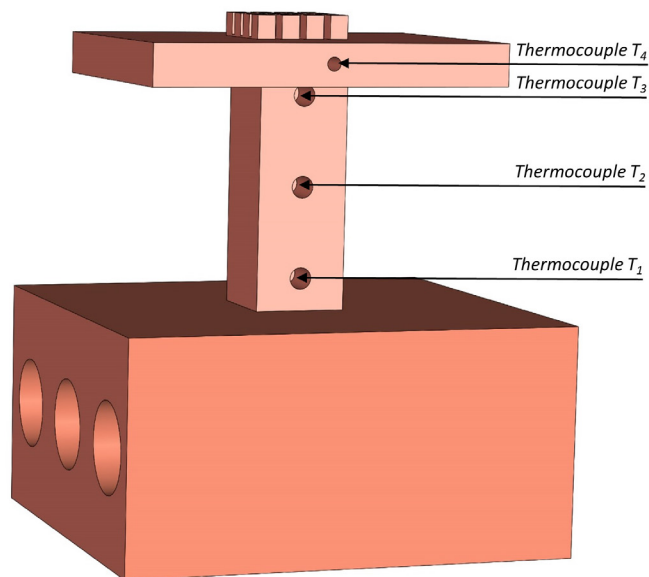


Figure 5.2: Thermocouple location in the 1D column.

$$q'' = -k_{Cu} \frac{dT}{dx} \quad (4)$$

where,

k_{Cu} = Conductivity of copper

$\frac{dT}{dx}$ = temperature gradient in along 1D column, calculated using three-point backward space Taylor series approximation

$$= \frac{3T_1 - 4T_2 + T_3}{2\Delta x}$$

Δx = distance between the center of the thermocouple holes

The Equation (5) for surface temperature is

$$T_s = T_4 - \frac{q'' dx}{k_{cu}} \quad (5)$$

Lastly, the heat transfer coefficient is given by Equation (6)

$$h = \frac{q''}{\Delta T_{sat}} \quad (6)$$

where,

$$\Delta T_{sat} = T_{surface} - T_{sat}$$

5.3 Uncertainty Analysis

Every experiment has certain amount of uncertainty associated with it. These uncertainties further propagate to parameters depending on measured quantities. Therefore, it is important to take this uncertainty into account for results and analysis. The uncertainty of a system is given by Equation (7)

$$E_y = \sqrt{S_y^2 + R_y^2} \quad (7)$$

Uncertainty has two error components in it, systematic error (or bias error, S_y) and random error (or precision error, R_y). The systematic error can be accounted to human error or fault in the calibration of instruments. Random error accounts to uncontrolled variables in the measurement process.

The uncertainty in this study is related to indirect measurement of heat flux and surface temperature. These parameters are interpolated using three parameters: temperature, lengths and conductivity of copper. For a k-type thermocouple, the uncertainty in temperature measurement was within ± 0.1 °C. Second source of uncertainty is in the thermal conductivity of copper as temperature changes, which was not provided by the manufacturer, thus taken to be constant. Lastly, the uncertainty in the measurement of lengths i.e. the spacing between the thermocouple is 1% which was determined via resolution of the measurement device used for measurement. The summary of uncertainty is shown in Table 5.1

Table 5.1: Values of uncertainties in various parameters

Parameter	Units	Parameter value	Uncertainty	% Uncertainty	Uncertainty value
k_{cu}	W/m-K	390.88	E_k	NA	NA
Δx	m	0.01	$E_{\Delta x}$	1	0.0001
T_1	°C	Varies	E_{T1}	NA	0.2
T_2	°C	Varies	E_{T2}	NA	0.2
T_3	°C	Varies	E_{T3}	NA	0.2
T_4	°C	Varies	E_{T4}	NA	0.2

These uncertainties might be small but when combined to evaluate other parameters, these can propagate to higher values. The two derived parameters in this study are heat flux and surface temperature. The heat flux and the surface temperature is affected by uncertainty in temperature, length and thermal conductivity of copper. The uncertainty propagated is given by rule of partial sums given Equation (8).

$$E_p = \sqrt{\sum \left(\frac{\partial p}{\partial \alpha} \right)^2 E_\alpha^2} \quad (8)$$

where,

p = parameter to be calculated

α = measured parameter

E_α = Uncertainty in the measured parameter

The uncertainty in the heat flux value can then be calculated by deriving the equation from Equation (7) and using Equation (8). Dividing by heat flux yields the percentage uncertainty in the heat flux which is given by Equation (9)

The percentage uncertainty associated with heat flux measurement can be modified into Equation (9):

$$\frac{E_{q''}}{q''} = \sqrt{\left(\frac{E_k}{k}\right)^2 + \left(\frac{3E_{T_1} * k_{cu}}{\Delta x * q''}\right)^2 + \left(\frac{4E_{T_2} * k_{cu}}{\Delta x * q''}\right)^2 + \left(\frac{E_{T_3} * k_{cu}}{\Delta x * q''}\right)^2 + \left(\frac{E_{\Delta x}}{\Delta x}\right)^2} \quad (9)$$

The percentage uncertainty in the calculation of wall superheat is given by Equation (10):

$$\frac{E_{\Delta T_{sat}}}{\Delta T_{sat}} = \sqrt{\left(\frac{E_{T_4}}{\Delta T_{sat}}\right)^2 + \left(\frac{\Delta x * E_{q''}}{k_{cu} * \Delta T_{sat}}\right)^2 + \left(\frac{q'' * E_{\Delta x}}{k_{cu} * \Delta T_{sat}}\right)^2} \quad (10)$$

The percentage uncertainty in the calculation of heat transfer coefficient is given by Equation (11):

$$\frac{E_h}{h} = \sqrt{\left(\frac{E_{q''}}{q''}\right)^2 + \left(\frac{E_{\Delta T}}{\Delta T}\right)^2} \quad (11)$$

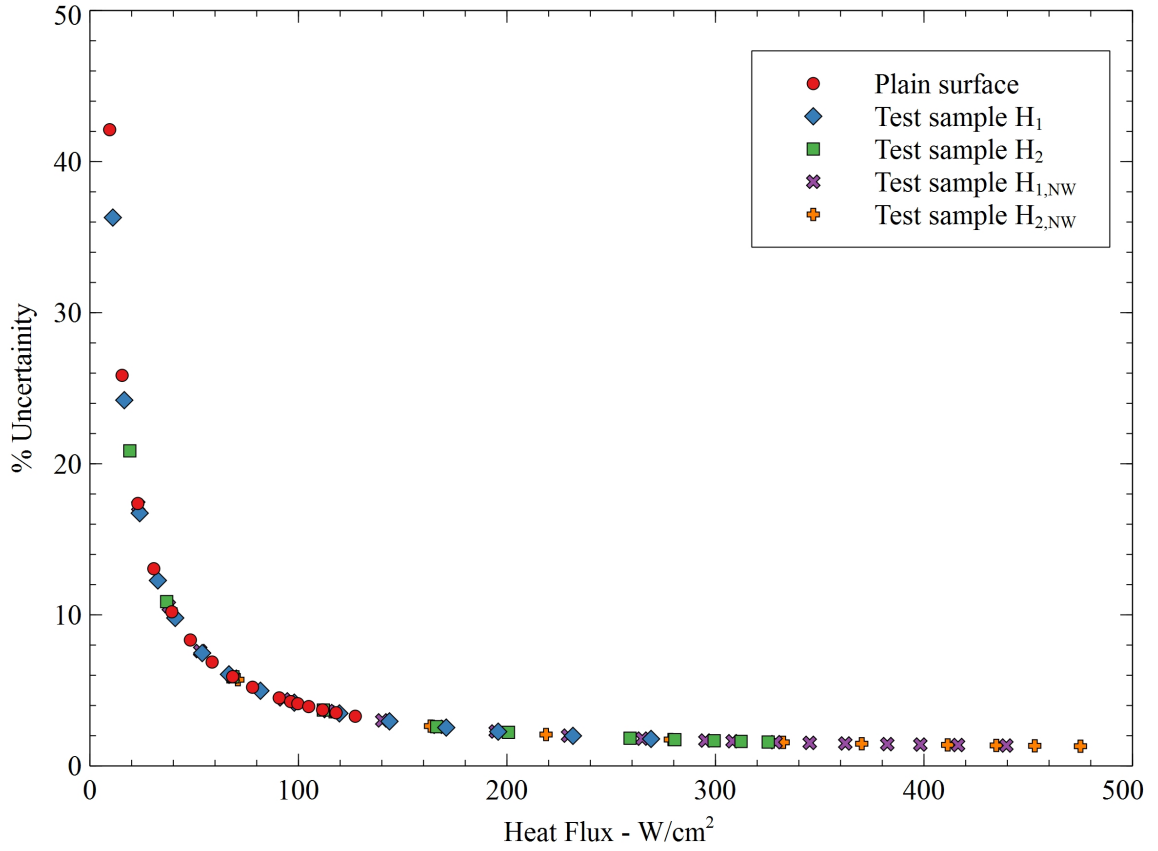


Figure 5.3: Graph indicating the percentage uncertainty at different heat flux values.

As seen from the Figure 5.3 , the uncertainties in reported heat flux range are within 5% uncertainty.

6 Results and Discussion

6.1 Effect of out-of-plane capillary wicking length scale on heat transfer performance.

To evaluate the performance of the test samples under study, pool boiling tests were conducted with de-ionized water under atmospheric pressure. Accordingly, performance of the test sample H_1 (equivalent to a height 1.4 mm) and H_2 (equivalent to a height 2.6 mm) were evaluated. Resultant plots of heat flux and heat transfer coefficient were plotted to see the trend in the boiling curve and overall heat transfer performance.

6.1.1 Effect of out-of-plane capillary wicking length scale on heat flux.

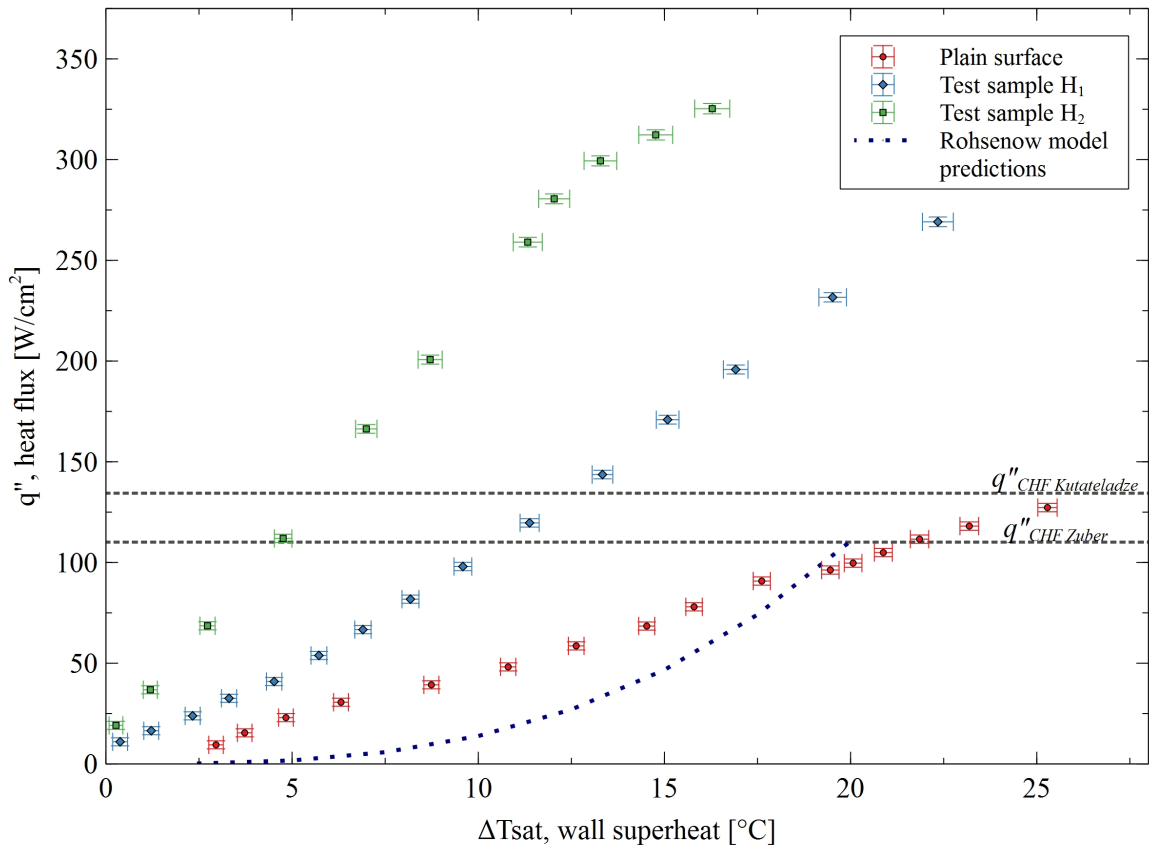


Figure 6.1: Heat flux as a function of wall superheat at different out-of-plane capillary wicking length scales.

The experimentally measured heat flux as a function of wall superheat for different test samples are shown in Figure 6.1. The baseline plain surface showed a CHF of 127.3 W/cm² at 25.3°C wall superheat. The experimental results for heat flux on plain copper surface is shown in dotted line with Rohsenow's heat flux model predictions, calculations for which are given in Appendix A.1. The experimental value of CHF for a plain copper surface lies between the predicted value of Kutateladze and Zuber, calculations for which are given in Appendix A.2. The figure clearly indicates the multi-scale capillary-assisted test surfaces of H₁ and H₂ outperform the plain surface with considerable higher measured heat fluxes at a given wall superheat. This can be attributed to the augmented active nucleation sites

and enhanced surface area that are offered by the structured porous matrix surfaces. Also, the complex porous matrix structures offer preferential out-of-plane wicking flow towards to the heater surface, which ensures additional liquid supply to the hotspots. Also, the structured pillar surfaces introduce separate vapor and liquid pathways, and thus reducing resistance for the formed vapor bubbles to escape from the bottom heated surface.

The effect of height is also clearly visible on the performance of the test samples. Test sample H₂ has a higher height as compared to the test sample H₁. The higher height offers the potential to augment active micro nucleation sites for bubble formation and heat transfer area, boosting the heat transfer process indicated by higher HTC and heat flux values. In addition, the test surface having a higher height can wick liquid from further far-field distance, and thus bridging thicker vapor films formed in the vicinity of CHF limit. This, subsequently, results in higher CHF values. At a wall superheat of 12.5°C, the heat flux enhancement offered by sample H₂ is approximately 90 percent over test sample H₁ and about 390 percent over the plain surface. Additionally, the highest heat flux was reported by the test sample H₂ is 325.3 W/cm² at 16.3 °C wall superheat. This is about 1.2 times and about 2.5 times enhancement in the CHF value over sample H₁ and plain surface respectively.

6.1.2 Effect of out-of-plane capillary wicking length scale on heat transfer coefficient.

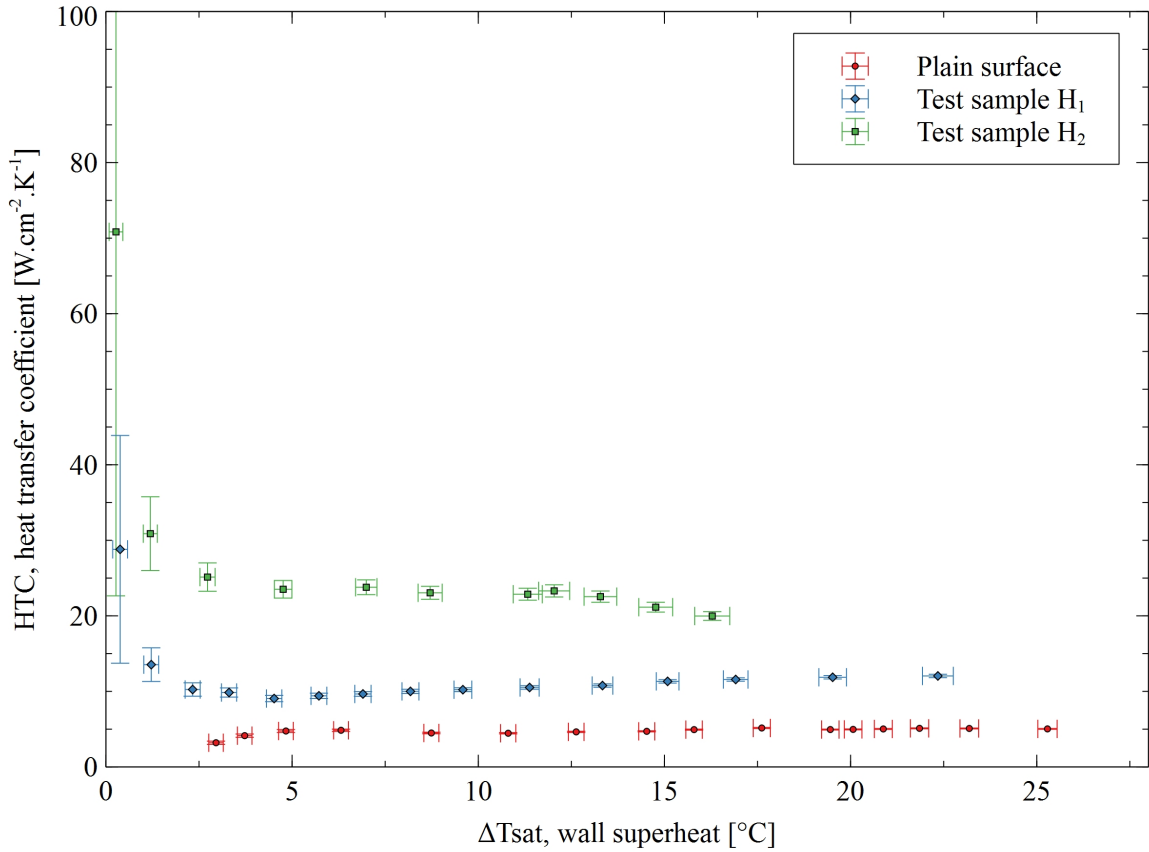


Figure 6.2: Heat transfer coefficient versus wall superheat for the test samples H₁ and H₂.

Second critical indicator of surface thermal performance is the heat transfer coefficient. Figure 6.2 indicates a plot of HTC against heat flux. The highest HTC was reported by the test sample H₂ as 70.8 W/cm²-K. The high HTC values at the beginning is accounted by the presence of very small wall superheats. At higher wall superheats, number of active bubble nucleation sites increases. If heat flux linearly increases at higher wall superheats, then the HTC remains constant. This trend can be seen at higher wall superheats.

6.2 Effect of growth of hierarchical structures on heat transfer performance.

The next step in this study was to grow nanowires on the structured copper meshes to form hierarchical surfaces. As discussed in the experimental section, the nanowires were grown via a chemical treatment on the test samples, and subsequently pool boiling experiments were carried out. The test samples $H_{1,NW}$ and $H_{2,NW}$ represent hierarchical boiling surfaces of the test samples H_1 and H_2 , respectively.

6.2.1 Effect of test sample H_1 and $H_{1,NW}$ with and without nanowires on heat flux.

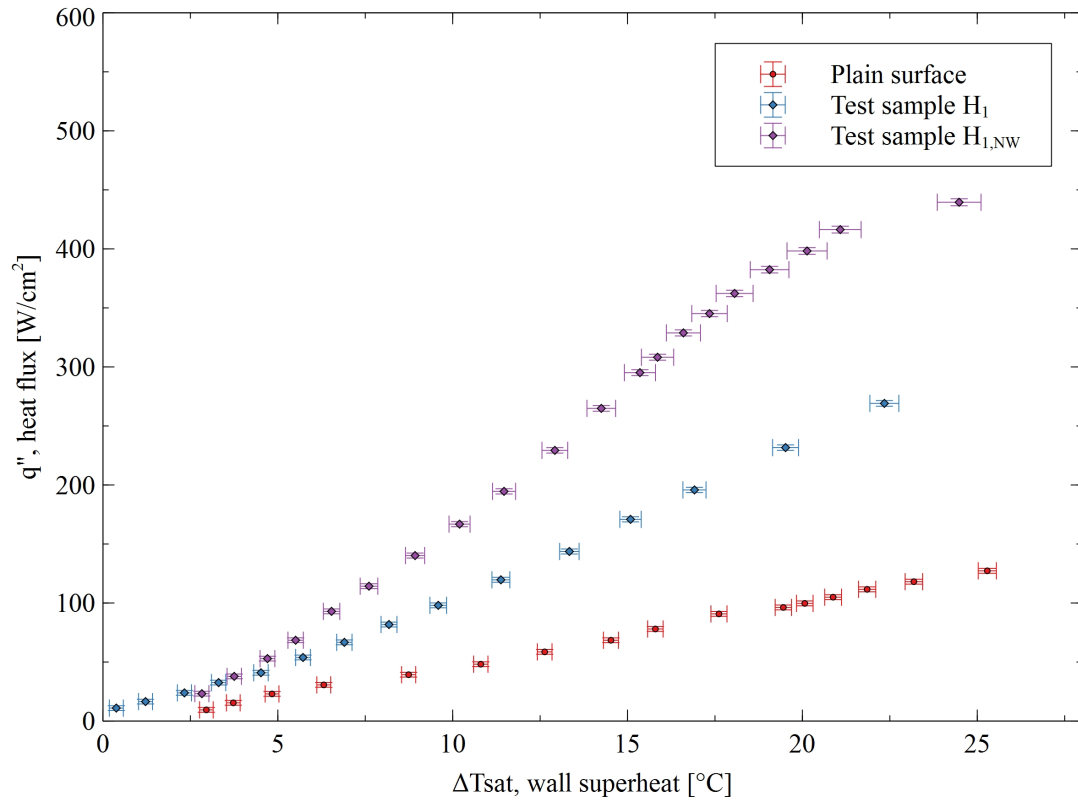


Figure 6.3: Heat flux as a function of wall superheat for the test samples H_1 and $H_{1,NW}$.

The effect of nanowire growth on overall heat transfer performance is clearly visible in Figure 6.3. Nanowire-grown capillary-assisted surfaces provide a higher wickability, extending duration of thin film evaporation mode of heat transfer during bubble growth and rewetting stages. Liquid wicked by the nanowires also stretch the complex three-phase solid-liquid-vapor contact line around the periphery of the bubble, thereby further augmenting thin film evaporation mode of heat transfer. In addition, nanowires alter surface wettability by reducing the liquid contact angle. A reduced contact angle leads to a thinner micro layer formed around bubble boundary on the solid surface, and thus amplifying thin film evaporation mechanism. As thin film evaporation is proposed to be a dominating heat transfer mechanism, its amplification leads to the observed enhancement in the heat transfer performance. At a wall superheat of 12.5 °C, the enhancement in the heat flux by the test sample $H_{1, NW}$ is about 46 percent over the test sample H_1 and about 280 percent over the plain surface. Also, the CHF observed by the test sample $H_{1, NW}$ is 439.5 W/cm², which is about 1.6 times and 3.4 times enhancement in heat flux values of the test sample H_1 and plain surfaces, respectively.

6.2.2 Effect of test sample H_2 and $H_{2,NW}$ with and without nanowires on heat flux.

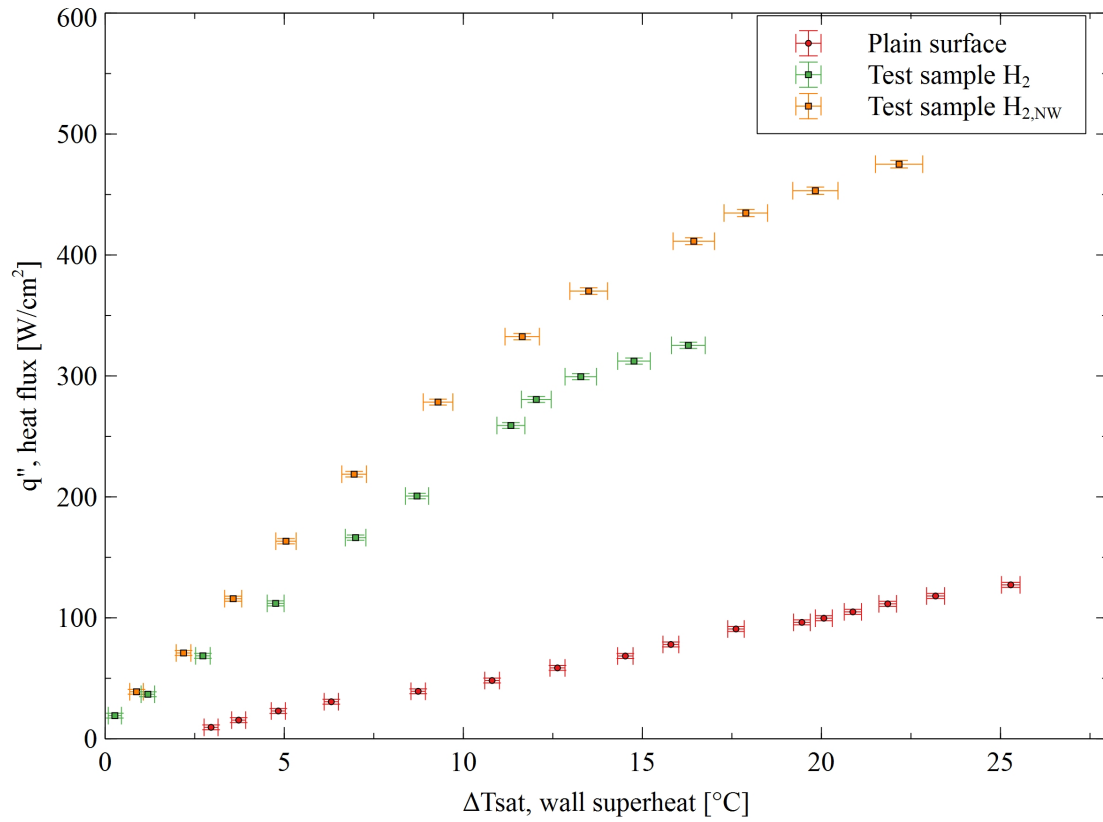


Figure 6.4a: Heat flux versus wall superheat for the test sample H_2 , $H_{2,NW}$, and plain surfaces.

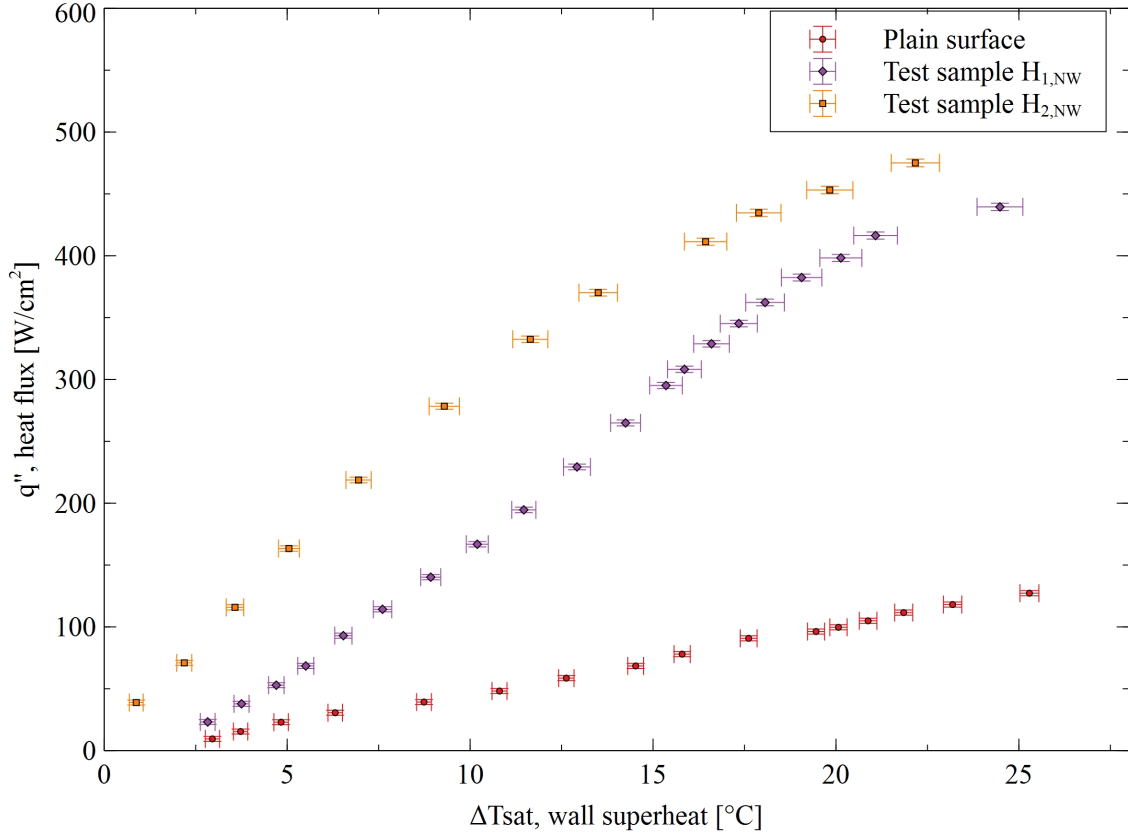


Figure 6.4b: Heat flux versus wall superheat for the test sample H_{1,NW}, H_{2,NW}, and plain surfaces.

Figure 6.4 a and b represent the effect of nanowire growth on the overall heat transfer performance for the test sample H₂. Similar to the H₁ and H_{1,NW} test surfaces, the H₂ and H_{2,NW} test samples demonstrate a considerable improvement in heat transfer as compared to the plain surface. However, at a much increased height, surface heat flux is highly amplified compared to the test surface H_{1,NW}. This can be attributed to the possibility of more active nucleation sites and added surface area at a higher height. This is in contrast to a solid pillar structure where its thermal efficiency significantly drops at higher heights. Here, the out-of-plane capillary wicking helps to maintain a high thermal performance at higher heights as evident in Figure 6.4 a and 6.4 b. At a wall superheat of 12.5°C, the enhancement in the heat flux by the test sample H_{2,NW} is approximately 20 percent over

the test sample H₂ and 500 percent over the plain surface. This resulted in highest CHF reported in this study for the test sample H_{2,NW} as 475 W/cm² at 22.2 °C wall superheat. For comparison, the CHF value reported by the test sample H_{2,NW} is about 1.46 times and 3.7 times over the test sample H₂ and plain surfaces, respectively.

6.2.3 Effect of test sample $H_{1,NW}$ and $H_{2,NW}$ on heat transfer coefficient.

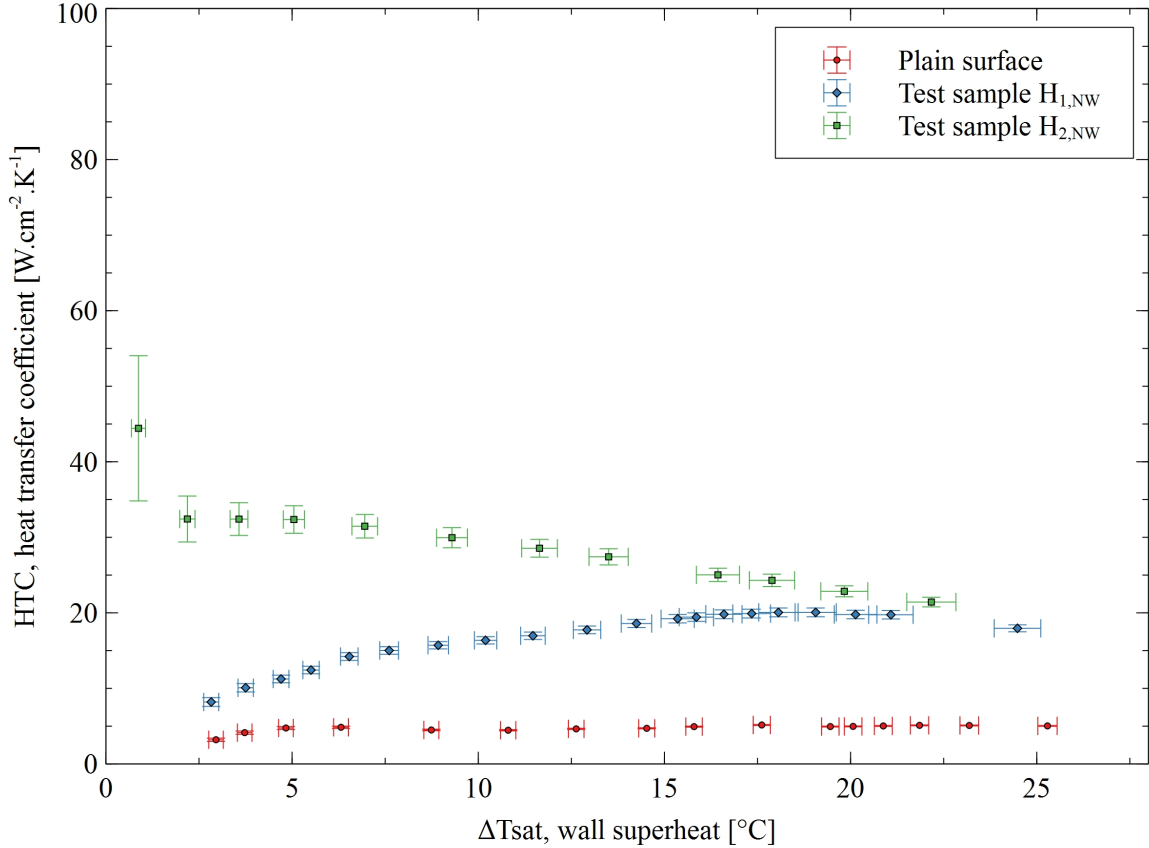


Figure 6.5: Heat transfer coefficient versus wall superheat for the test samples with nanowires $H_{1,NW}$ and $H_{2,NW}$.

The HTC graph for the nanowire grown structures is represented in Figure 6.5. As shown, the test surface $H_{2,NW}$ has a higher heat transfer coefficient compared to the test sample $H_{1,NW}$. This is attributed to a higher heat flux associated with the test sample $H_{2,NW}$ owing to its added surface area and potential present of more active nucleation sites augmented with efficient out-of-plane capillary wicking.

7 Conclusion

In conclusion, this work represents results of pool boiling experiments on sintered copper porous surfaces. Pool boiling tests were conducted to study effect of out-of-plane capillary wicking length scale on overall heat transfer rate. In addition, nanowires were grown on the test samples via a chemical treatment process to elucidate the effect of micro-nano hierarchical structures on boiling process. Following are key observations made during this study:

1. Sintered, porous hybrid structures were successfully fabricated using copper meshes sintered via a custom-made diffusion bonding setup. Two samples with 6-layers (i.e. equivalent to a height of 1.4 mm) and 12 layers (i.e., a height of 2.6 mm) were diffusion bonded and machined to form structured micro-pillar surfaces. Additionally, nanowires were grown on these porous structures using a chemical treatment process which transformed the surfaces into superhydrophilic surfaces.
2. Pool boiling experiments were conducted using de-ionized water as a working fluid and boiling curve were predicted for the samples to study the performance of these surfaces. Both CHF and HTC were greatly affected by the introduction of porous surfaces. The best samples reported 475 W/cm^2 CHF and $70.8 \text{ W/cm}^2\text{-K}$ HTC.
3. The enhancement can be attributed to: a) augmented roughness increasing nucleation site densities and wetted surface area, b) capillary pumping aiding in supplemental liquid supply by in and out-of-plane capillary wicking, and c) structured micro-pillars providing separate reduced-resistance pathways for liquid and vapor phases.

8 Future Scope

The test samples evaluated for this study prove the importance of out-of-plane capillary wicking in addition to nucleation site density, wettability and in-plane wickability offered by different surface enhancements. We are yet to exploit the huge potential might be offered by these surface enhancements to augment the overall pool boiling heat transfer performance. Further optimization of the surface topology and development of a characteristic model can aid in understanding the effect of each parameter in more details. Future experiments can be conducted with varying pore sizes of the copper meshes, material and number of layers. The dimensions of the features such as width, spacing and height can also be altered to better understand their effect on the performance.

9 Reference List

- [1] Anderson, T.M., Mudawar, I., 1989, "Microelectronic Cooling by Enhanced Pool Boiling of a Dielectric Fluorocarbon Liquid", *Journal of Heat Transfer*, 111(3) 752-759, Retrieved:<https://doi.org/10.1115/1.3250747>.
- [2] You, S.M., Simon, T.W., Bar-Cohen, A., 1992, "A technique for enhancing boiling heat transfer with application to cooling of electronic equipment", *IEEE Transactions on Components, Hybrids, and Manufacturing Technology*, 15(5) 823-831, Retrieved:<https://doi.org/10.1109/33.180048>.
- [3] Honda, H., Wei, J.J., 2004, "Enhanced boiling heat transfer from electronic components by use of surface microstructures", *Experimental Thermal and Fluid Science*, 28(2) 159-169, Retrieved:[https://doi.org/10.1016/S0894-1777\(03\)00035-9](https://doi.org/10.1016/S0894-1777(03)00035-9).
- [4] Mudawar, I., 2011, "Two-Phase Microchannel Heat Sinks: Theory, Applications, and Limitations", *Journal of Electronic Packaging*, 133(4) 041002-041002-041031, Retrieved:<https://doi.org/10.1115/1.4005300>.
- [5] Nadjahi, C., Louahlia, H., Lemasson, S., 2018, "A review of thermal management and innovative cooling strategies for data center", *Sustainable Computing: Informatics and Systems*, 19 14-28, Retrieved:<https://doi.org/10.1016/j.suscom.2018.05.002>.
- [6] Chauhan, A., Kandlikar, S.G., 2019, "Characterization of a dual taper thermosiphon loop for CPU cooling in data centers", *Applied Thermal Engineering*, 146 450-458, Retrieved:<https://doi.org/10.1016/j.applthermaleng.2018.10.010>.
- [7] Li, Z., Kandlikar, S.G., 2015, "Current Status and Future Trends in Data-Center Cooling Technologies", *Heat Transfer Engineering*, 36(6) 523-538, Retrieved:<https://doi.org/10.1080/01457632.2014.939032>.
- [8] Ebrahimi, K., Jones, G.F., Fleischer, A.S., 2014, "A review of data center cooling technology, operating conditions and the corresponding low-grade waste heat recovery opportunities", *Renewable and Sustainable Energy Reviews*, 31 622-638, Retrieved:<https://doi.org/10.1016/j.rser.2013.12.007>.
- [9] Mercado, M., Wong, N., Hartwig, J., 2019, "Assessment of two-phase heat transfer coefficient and critical heat flux correlations for cryogenic flow boiling in pipe heating experiments", *International Journal of Heat and Mass Transfer*, 133 295-315, Retrieved:<https://doi.org/10.1016/j.ijheatmasstransfer.2018.12.108>.
- [10] Delil, A.A.M., Two-Phase Heat Transport Systems for Spacecraft-Scaling with Respect to Gravity, in, *SAE International*, 1989.

- [11] Park, C., Vallury, A., Zuo, J., Perez, J., Rogers, P., 2007, "Spacecraft Thermal Management Using Advanced Hybrid Two-Phase Loop Technology", *AIP Conference Proceedings*, 880(1) 11-18, Retrieved:<https://doi.org/10.1063/1.2437435>.
- [12] Wei, A., Qu, J., Qiu, H., Wang, C., Cao, G., 2019, "Heat transfer characteristics of plug-in oscillating heat pipe with binary-fluid mixtures for electric vehicle battery thermal management", *International Journal of Heat and Mass Transfer*, 135 746-760, Retrieved:<https://doi.org/10.1016/j.ijheatmasstransfer.2019.02.021>.
- [13] Al-Zareer, M., Dincer, I., Rosen, M.A., 2018, "Development and evaluation of a new ammonia boiling based battery thermal management system", *Electrochimica Acta*, 280 340-352, Retrieved:<https://doi.org/10.1016/j.electacta.2018.05.093>.
- [14] Xia, G., Cao, L., Bi, G., 2017, "A review on battery thermal management in electric vehicle application", *Journal of Power Sources*, 367 90-105, Retrieved:<https://doi.org/10.1016/j.jpowsour.2017.09.046>.
- [15] Lasance, C.J.M., *Advances In High-Performance Cooling For Electronics*, in: *Electronics Cooling*, 2005.
- [16] Anandan, S., Ramalingam, V., 2008, "Thermal management of electronics: A review of literature", *Thermal Science*, 12(2) 5-26, Retrieved:<https://doi.org/10.2298/tsci0802005a>.
- [17] Dhir, V.K., 1998, "BOILING HEAT TRANSFER", *Annual Review of Fluid Mechanics*, 30(1) 365-401, Retrieved:<https://doi.org/10.1146/annurev.fluid.30.1.365>.
- [18] Liang, G., Mudawar, I., 2019, "Review of pool boiling enhancement by surface modification", *International Journal of Heat and Mass Transfer*, 128 892-933, Retrieved:<https://doi.org/10.1016/j.ijheatmasstransfer.2018.09.026>.
- [19] Lu, Y.-W., Kandlikar, S.G., 2011, "Nanoscale Surface Modification Techniques for Pool Boiling Enhancement—A Critical Review and Future Directions", *Heat Transfer Engineering*, 32(10) 827-842, Retrieved:<https://doi.org/10.1080/01457632.2011.548267>.
- [20] Shiro, N., 1984, "The maximum and minimum values of the heat q transmitted from metal to boiling water under atmospheric pressure", *International Journal of Heat and Mass Transfer*, 27(7) 959-970, Retrieved:[https://doi.org/10.1016/0017-9310\(84\)90112-1](https://doi.org/10.1016/0017-9310(84)90112-1).
- [21] Bergman, T.L., Incropera, F.P., DeWitt, D.P., Lavine, A.S., *Fundamentals of heat and mass transfer*, John Wiley & Sons, 2011.
- [22] Carey, V.P., *Liquid vapor phase change phenomena: an introduction to the thermophysics of vaporization and condensation processes in heat transfer equipment*, CRC Press, 2018.

- [23] Hsu, Y.Y., 1962, "On the Size Range of Active Nucleation Cavities on a Heating Surface", *Journal of Heat Transfer*, 84(3) 207-213, Retrieved:<https://doi.org/10.1115/1.3684339>.
- [24] Li, C., Wang, Z., Wang, P.I., Peles, Y., Koratkar, N., Peterson, G.P., 2008, "Nanostructured copper interfaces for enhanced boiling", *Small*, 4(8) 1084-1088, Retrieved:<https://doi.org/10.1002/sml.200700991>.
- [25] Rohsenow, W.M., A METHOD OF CORRELATING HEAT TRANSFER DATA FOR SURFACE BOILING OF LIQUIDS. (Technical Report No. 5), Country unknown/Code not available, 1951.
- [26] Mikic, B.B., Rohsenow, W.M., Griffith, P., 1970, "On bubble growth rates", *International Journal of Heat and Mass Transfer*, 13(4) 657-666, Retrieved:[https://doi.org/10.1016/0017-9310\(70\)90040-2](https://doi.org/10.1016/0017-9310(70)90040-2).
- [27] Judd, R.L., Hwang, K.S., 1976, "A Comprehensive Model for Nucleate Pool Boiling Heat Transfer Including Microlayer Evaporation", *Journal of Heat Transfer*, 98(4) 623-629, Retrieved:<https://doi.org/10.1115/1.3450610>.
- [28] Haramura, Y., Katto, Y., 1983, "A new hydrodynamic model of critical heat flux, applicable widely to both pool and forced convection boiling on submerged bodies in saturated liquids", *International Journal of Heat and Mass Transfer*, 26(3) 389-399, Retrieved:[https://doi.org/10.1016/0017-9310\(83\)90043-1](https://doi.org/10.1016/0017-9310(83)90043-1).
- [29] Kandlikar, S.G., 2001, "A Theoretical Model to Predict Pool Boiling CHF Incorporating Effects of Contact Angle and Orientation", *Journal of Heat Transfer*, 123(6) 1071-1079, Retrieved:<https://doi.org/10.1115/1.1409265>.
- [30] Gerardi, C., Buongiorno, J., Hu, L.-w., McKrell, T., 2010, "Study of bubble growth in water pool boiling through synchronized, infrared thermometry and high-speed video", *International Journal of Heat and Mass Transfer*, 53(19) 4185-4192, Retrieved:<https://doi.org/10.1016/j.ijheatmasstransfer.2010.05.041>.
- [31] Bigham, S., Fazeli, A., Moghaddam, S., 2017, "Physics of microstructures enhancement of thin film evaporation heat transfer in microchannels flow boiling", *Sci Rep*, 7 44745, Retrieved:<https://doi.org/10.1038/srep44745>.
- [32] Moghaddam, S., Kiger, K., 2009, "Physical mechanisms of heat transfer during single bubble nucleate boiling of FC-72 under saturation conditions. II: Theoretical analysis", *International Journal of Heat and Mass Transfer*, 52(5) 1295-1303, Retrieved:<https://doi.org/10.1016/j.ijheatmasstransfer.2008.08.024>.
- [33] Kim, J., 2009, "Review of nucleate pool boiling bubble heat transfer mechanisms", *International Journal of Multiphase Flow*, 35(12) 1067-1076, Retrieved:<https://doi.org/10.1016/j.ijmultiphaseflow.2009.07.008>.

- [34] O'Hanley, H., Coyle, C., Buongiorno, J., McKrell, T., Hu, L.-W., Rubner, M., Cohen, R., 2013, "Separate effects of surface roughness, wettability, and porosity on the boiling critical heat flux", *Applied Physics Letters*, 103(2), Retrieved:<https://doi.org/10.1063/1.4813450>.
- [35] Guglielmini, G., Misale, M., Schenone, C., 2002, "Boiling of saturated FC-72 on square pin fin arrays", *International Journal of Thermal Sciences*, 41(7) 599-608, Retrieved:[https://doi.org/10.1016/S1290-0729\(02\)01353-4](https://doi.org/10.1016/S1290-0729(02)01353-4).
- [36] Wei, J.J., Honda, H., 2003, "Effects of fin geometry on boiling heat transfer from silicon chips with micro-pin-fins immersed in FC-72", *International Journal of Heat and Mass Transfer*, 46(21) 4059-4070, Retrieved:[https://doi.org/10.1016/s0017-9310\(03\)00226-6](https://doi.org/10.1016/s0017-9310(03)00226-6).
- [37] Zhang, M., Lian, K., 2008, "Using bulk micromachined structures to enhance pool boiling heat transfer", *Microsystem Technologies*, 14(9-11) 1499-1505, Retrieved:<https://doi.org/10.1007/s00542-007-0531-x>.
- [38] Chu, K.-H., Enright, R., Wang, E.N., 2012, "Structured surfaces for enhanced pool boiling heat transfer", *Applied Physics Letters*, 100(24), Retrieved:<https://doi.org/10.1063/1.4724190>.
- [39] Kim, S.H., Lee, G.C., Kang, J.Y., Moriyama, K., Kim, M.H., Park, H.S., 2015, "Boiling heat transfer and critical heat flux evaluation of the pool boiling on micro structured surface", *International Journal of Heat and Mass Transfer*, 91 1140-1147, Retrieved:<https://doi.org/10.1016/j.ijheatmasstransfer.2015.07.120>.
- [40] Kim, D.E., Yu, D.I., Park, S.C., Kwak, H.J., Ahn, H.S., 2015, "Critical heat flux triggering mechanism on micro-structured surfaces: Coalesced bubble departure frequency and liquid furnishing capability", *International Journal of Heat and Mass Transfer*, 91 1237-1247, Retrieved:<https://doi.org/10.1016/j.ijheatmasstransfer.2015.08.065>.
- [41] Forrest, E., Williamson, E., Buongiorno, J., Hu, L.-W., Rubner, M., Cohen, R., 2010, "Augmentation of nucleate boiling heat transfer and critical heat flux using nanoparticle thin-film coatings", *International Journal of Heat and Mass Transfer*, 53(1-3) 58-67, Retrieved:<https://doi.org/10.1016/j.ijheatmasstransfer.2009.10.008>.
- [42] Feng, B., Weaver, K., Peterson, G.P., 2012, "Enhancement of critical heat flux in pool boiling using atomic layer deposition of alumina", *Applied Physics Letters*, 100(5), Retrieved:<https://doi.org/10.1063/1.3681943>.
- [43] Ali, A.F., El-Genk, M.S., 2012, "Effect of inclination on saturation boiling of PF-5060 dielectric liquid on 80- and 137- μm thick copper micro-porous surfaces", *International Journal of Thermal Sciences*, 53 42-48, Retrieved:<https://doi.org/10.1016/j.ijthermalsci.2011.11.004>.

- [44] Li, S., Furberg, R., Toprak, M.S., Palm, B., Muhammed, M., 2008, "Nature-Inspired Boiling Enhancement by Novel Nanostructured Macroporous Surfaces", *Advanced Functional Materials*, 18(15) 2215-2220, Retrieved:<https://doi.org/10.1002/adfm.200701405>.
- [45] Zhang, B.J., Kim, K.J., Yoon, H., 2012, "Enhanced heat transfer performance of alumina sponge-like nano-porous structures through surface wettability control in nucleate pool boiling", *International Journal of Heat and Mass Transfer*, 55(25-26) 7487-7498, Retrieved:<https://doi.org/10.1016/j.ijheatmasstransfer.2012.07.053>.
- [46] Ahn, H.S., Kim, J.M., Park, C., Jang, J.W., Lee, J.S., Kim, H., Kaviany, M., Kim, M.H., 2013, "A novel role of three dimensional graphene foam to prevent heater failure during boiling", *Sci Rep*, 3 1960, Retrieved:<https://doi.org/10.1038/srep01960>.
- [47] Li, C., Peterson, G.P., 2007, "Parametric Study of Pool Boiling on Horizontal Highly Conductive Microporous Coated Surfaces", *Journal of Heat Transfer*, 129(11) 1465-1475, Retrieved:<https://doi.org/10.1115/1.2759969>.
- [48] Yang, Y., Ji, X., Xu, J., 2010, "Pool boiling heat transfer on copper foam covers with water as working fluid", *International Journal of Thermal Sciences*, 49(7) 1227-1237, Retrieved:<https://doi.org/10.1016/j.ijthermalsci.2010.01.013>.
- [49] Wong, K.K., Leong, K.C., 2018, "Saturated pool boiling enhancement using porous lattice structures produced by Selective Laser Melting", *International Journal of Heat and Mass Transfer*, 121 46-63, Retrieved:<https://doi.org/10.1016/j.ijheatmasstransfer.2017.12.148>.
- [50] Chen, R., Lu, M.-C., Srinivasan, V., Wang, Z., Cho, H.H., Majumdar, A., 2009, "Nanowires for Enhanced Boiling Heat Transfer", *Nano Letters*, 9(2) 548-553, Retrieved:<https://doi.org/10.1021/nl8026857>.
- [51] Yao, Z., Lu, Y.W., Kandlikar, S.G., 2011, "Effects of nanowire height on pool boiling performance of water on silicon chips", *International Journal of Thermal Sciences*, 50(11) 2084-2090, Retrieved:<https://doi.org/10.1016/j.ijthermalsci.2011.06.009>.
- [52] Udaya Kumar, G., Suresh, S., Thansekhar, M.R., Halpati, D., 2018, "Role of inter-nanowire distance in metal nanowires on pool boiling heat transfer characteristics", *J Colloid Interface Sci*, 532 218-230, Retrieved:<https://doi.org/10.1016/j.jcis.2018.07.092>.
- [53] Deng, D., Feng, J., Huang, Q., Tang, Y., Lian, Y., 2016, "Pool boiling heat transfer of porous structures with reentrant cavities", *International Journal of Heat and Mass Transfer*, 99 556-568, Retrieved:<https://doi.org/10.1016/j.ijheatmasstransfer.2016.04.015>.
- [54] Liter, S.G., Kaviany, M., 2001, "Pool-boiling CHF enhancement by modulated porous-layer coating: theory and experiment", *International Journal of Heat and Mass Transfer*, 44(22) 4287-4311, Retrieved:[https://doi.org/10.1016/S0017-9310\(01\)00084-9](https://doi.org/10.1016/S0017-9310(01)00084-9).

- [55] Li, C.H., Li, T., Hodgins, P., Hunter, C.N., Voevodin, A.A., Jones, J.G., Peterson, G.P., 2011, "Comparison study of liquid replenishing impacts on critical heat flux and heat transfer coefficient of nucleate pool boiling on multiscale modulated porous structures", *International Journal of Heat and Mass Transfer*, 54(15-16) 3146-3155, Retrieved:<https://doi.org/10.1016/j.ijheatmasstransfer.2011.03.062>.
- [56] Chu, K.-H., Soo Joung, Y., Enright, R., Buie, C.R., Wang, E.N., 2013, "Hierarchically structured surfaces for boiling critical heat flux enhancement", *Applied Physics Letters*, 102(15), Retrieved:<https://doi.org/10.1063/1.4801811>.
- [57] Rahman, M.M., Olceroglu, E., McCarthy, M., 2014, "Role of wickability on the critical heat flux of structured superhydrophilic surfaces", *Langmuir*, 30(37) 11225-11234, Retrieved:<https://doi.org/10.1021/la5030923>.
- [58] Dhillon, N.S., Buongiorno, J., Varanasi, K.K., 2015, "Critical heat flux maxima during boiling crisis on textured surfaces", *Nat Commun*, 6 8247, Retrieved:<https://doi.org/10.1038/ncomms9247>.
- [59] Kandlikar, S.G., 2013, "Controlling bubble motion over heated surface through evaporation momentum force to enhance pool boiling heat transfer", *Applied Physics Letters*, 102(5), Retrieved:<https://doi.org/10.1063/1.4791682>.
- [60] Ashworth, M.A., Jacobs, M.H., Davies, S., 2000, "Basic mechanisms and interface reactions in HIP diffusion bonding", *Materials & Design*, 21(4) 351-358, Retrieved:[https://doi.org/10.1016/S0261-3069\(99\)00088-6](https://doi.org/10.1016/S0261-3069(99)00088-6).
- [61] Huang, D.-J., Leu, T.-S., 2013, "Fabrication of high wettability gradient on copper substrate", *Applied Surface Science*, 280 25-32, Retrieved:<https://doi.org/10.1016/j.apsusc.2013.04.065>.
- [62] Kutateladze, S., 1951, "HYDRODYNAMIC THEORY OF VARIATIONS IN RATE OF BOILING OF LIQUIDS UNDER FREE CONVECTION", *Izvest. Akad. Nauk SSSR, Otdel. Tekh. Nauk*,
- [63] Zuber, N., Hydrodynamic aspects of boiling heat transfer (thesis), Ramo-Wooldridge Corp., Los Angeles, CA (United States); Univ. of California ..., 1959.

A Calculations

The calculation used for predicting the heat flux and CHF for plain surface are provided in the subsequent section

A.1 Calculation of Heat flux as predicted by Rohsenov model

The calculations of heat flux for a polished, plain copper surface is given by Rohsenov's [25] heat flux prediction model. For comparison with experimental results, the surface: fluid combination is taken as water as the working fluid and plain copper substrate as the surface. All properties are evaluated at saturation temperature (100°C) for atmospheric pressure. The equation for heat flux in relation to various thermos-physical properties of water and water vapor is given by

$$q'' = \mu_\ell h_{\ell v} \left[\frac{g(\rho_\ell - \rho_v)}{\sigma} \right]^{\frac{1}{2}} \left[\frac{c_{p\ell}(T_w - T_{sat})}{C_{s,\ell} h_{\ell v} \text{Pr}_\ell^n} \right]^3$$

A.2 Calculation of maximum heat flux as predicted by Kutateladze and Zuber

Based on the hydrodynamic instability model theory, the equation for Critical heat flux prediction is given by

$$q''_c = K \times h_{fg} \rho_g^{1/2} [\sigma h g (\rho_l - \rho_g)]^{1/4}$$

The value of constant $K = 0.16$, given by Kutateladze [62] and $K = 0.131$, given by Zuber [63]. The calculations of heat flux and CHF are done in Engineering Equation Solver (EES, Version 10.450, #1614) and is as shown below:

"1. Evaluation of heat flux based on Rohsenov model"

"All properties are evaluated at saturation temperature of 100°C at atmospheric pressure"

mu_l = 0.0002816 [Pa-s]	"viscosity of water"
C_sl = 0.013	"water-copper combination constant"
h_lv = 2256.4 [kJ/kg]	"latent heat of vaporization for water"
rho_l = 958.35 [kg/m^3]	"density of water"
rho_v = 0.59 [kg/m^3]	"density of water vapor"
sigma = 0.0588 [N/m]	"surface tension of water"
g = 9.81 [m/s^2]	"acceleration"
c_pl = 4.2157 [kJ/kg-K]	"specific heat of water"
Pr = 1.76	"Prandtl number for water "
n = 1	"water n constant"
T_sat = 100 [°C]	"saturation temperature at atmospheric pressure"
T_w[1..8] = [102.5 [K] ,105 [K] ,107.5 [K] ,110 [K] ,112.5 [K] ,115 [K] ,117.5 [K] ,120 [K]]	"wall superheat values"

"Heat flux values at various wall superheat"

$q[1] = \mu_l * h_{lv} * ((g * (\rho_l - \rho_v) / \sigma) ^ {1/2}) * ((c_{pl} * (T_w[1] - T_{sat})) / (C_{sl} * h_{lv} * (Pr^n))) ^ 3 / 10$ [W/cm^2]
 $q[2] = \mu_l * h_{lv} * ((g * (\rho_l - \rho_v) / \sigma) ^ {1/2}) * ((c_{pl} * (T_w[2] - T_{sat})) / (C_{sl} * h_{lv} * (Pr^n))) ^ 3 / 10$ [W/cm^2]
 $q[3] = \mu_l * h_{lv} * ((g * (\rho_l - \rho_v) / \sigma) ^ {1/2}) * ((c_{pl} * (T_w[3] - T_{sat})) / (C_{sl} * h_{lv} * (Pr^n))) ^ 3 / 10$ [W/cm^2]
 $q[4] = \mu_l * h_{lv} * ((g * (\rho_l - \rho_v) / \sigma) ^ {1/2}) * ((c_{pl} * (T_w[4] - T_{sat})) / (C_{sl} * h_{lv} * (Pr^n))) ^ 3 / 10$ [W/cm^2]
 $q[5] = \mu_l * h_{lv} * ((g * (\rho_l - \rho_v) / \sigma) ^ {1/2}) * ((c_{pl} * (T_w[5] - T_{sat})) / (C_{sl} * h_{lv} * (Pr^n))) ^ 3 / 10$ [W/cm^2]
 $q[6] = \mu_l * h_{lv} * ((g * (\rho_l - \rho_v) / \sigma) ^ {1/2}) * ((c_{pl} * (T_w[6] - T_{sat})) / (C_{sl} * h_{lv} * (Pr^n))) ^ 3 / 10$ [W/cm^2]
 $q[7] = \mu_l * h_{lv} * ((g * (\rho_l - \rho_v) / \sigma) ^ {1/2}) * ((c_{pl} * (T_w[7] - T_{sat})) / (C_{sl} * h_{lv} * (Pr^n))) ^ 3 / 10$ [W/cm^2]
 $q[8] = \mu_l * h_{lv} * ((g * (\rho_l - \rho_v) / \sigma) ^ {1/2}) * ((c_{pl} * (T_w[8] - T_{sat})) / (C_{sl} * h_{lv} * (Pr^n))) ^ 3 / 10$ [W/cm^2]

"2. Maximum heat flux (q_CHF) predictions based on Kutateladze and Zuber model"

"Kutateladze model CHF prediction, K = 0.16"

"Zuber model CHF prediction, K = 0.131"

K_Kut = 0.16

K_Zub = 0.131

$q_{CHF_Kut} = K_{Kut} * h_{lv} * (\rho_v^{0.5}) * ((\sigma * g * (\rho_l - \rho_v))^{1/4}) / 10$ [W/cm^2]
 $q_{CHF_Zub} = K_{Zub} * h_{lv} * (\rho_v^{0.5}) * ((\sigma * g * (\rho_l - \rho_v))^{1/4}) / 10$ [W/cm^2]

SOLUTION

Unit Settings: SI C kPa kJ mass deg

Cpl = 4.216 [kJ/kg-K]	Csl = 0.013
g = 9.81 [m/s^2]	hlv = 2256 [kJ/kg]
KKut = 0.16	KZub = 0.131
mu_l = 0.0002816 [Pa-s]	n = 1
Pr = 1.76	qCHF,Kut = 134.4 [W/cm^2]
qCHF,Zub = 110.1 [W/cm^2]	rho_l = 958.4 [kg/m^3]
rho_v = 0.59 [kg/m^3]	sigma = 0.0588 [N/m]
Tsat = 100 [°C]	

Arrays Table: Main

	q_i	$T_{w,i}$ [K]
1	0.2161	102.5
2	1.729	105
3	5.834	107.5
4	13.83	110
5	27.01	112.5

Arrays Table: Main

	q_i	$T_{w,i}$ [K]
6	46.68	115
7	74.12	117.5
8	110.6	120

B Copyright documentation

All figures used in the literature review section of this thesis are used after obtaining respective permission from the original journal publications. Copyright of such figures have been duly cited in the section to credit the original author and article.

Figure 1.4, Kim, J., 2009, "Review of nucleate pool boiling bubble heat transfer mechanisms", *International Journal of Multiphase Flow*, 35(12) 1067-1076, Retrieved:<https://doi.org/10.1016/j.ijmultiphaseflow.2009.07.008>. Permission purchase order number: 4590401117860.

Figure 2.1, Wei, J.J., Honda, H., 2003, "Effects of fin geometry on boiling heat transfer from silicon chips with micro-pin-fins immersed in FC-72", *International Journal of Heat and Mass Transfer*, 46(21) 4059-4070, Retrieved:[https://doi.org/10.1016/s0017-9310\(03\)00226-6](https://doi.org/10.1016/s0017-9310(03)00226-6). Permission purchase order number: 4590491506604.

Figure 2.2, Zhang, M., Lian, K., 2008, "Using bulk micromachined structures to enhance pool boiling heat transfer", *Microsystem Technologies*, 14(9-11) 1499-1505, Retrieved:<https://doi.org/10.1007/s00542-007-0531-x>. Permission purchase order number: 4590500320430.

Figure 2.3, Chu, K.-H., Enright, R., Wang, E.N., 2012, "Structured surfaces for enhanced pool boiling heat transfer", *Applied Physics Letters*, 100(24), Retrieved:<https://doi.org/10.1063/1.4724190>. Permission purchase order number: 4590501306647.

Figure 2.4, Kim, S.H., Lee, G.C., Kang, J.Y., Moriyama, K., Kim, M.H., Park, H.S., 2015, "Boiling heat transfer and critical heat flux evaluation of the pool boiling on micro structured surface", *International Journal of Heat and Mass Transfer*, 91 1140-1147, Retrieved:<https://doi.org/10.1016/j.ijheatmasstransfer.2015.07.120>. Permission purchase order number: 4590501471701.

Figure 2.5, Kim, D.E., Yu, D.I., Park, S.C., Kwak, H.J., Ahn, H.S., 2015, "Critical heat flux triggering mechanism on micro-structured surfaces: Coalesced bubble departure frequency and liquid furnishing capability", *International Journal of Heat and Mass Transfer*, 91 1237-1247, Retrieved:<https://doi.org/10.1016/j.ijheatmasstransfer.2015.08.065>. Permission purchase order number: 4590510061774.

Figure 2.6, Forrest, E., Williamson, E., Buongiorno, J., Hu, L.-W., Rubner, M., Cohen, R., 2010, "Augmentation of nucleate boiling heat transfer and critical heat flux using nanoparticle thin-film coatings", *International Journal of Heat and Mass Transfer*, 53(1-

3) 58-67, Retrieved:<https://doi.org/10.1016/j.ijheatmasstransfer.2009.10.008>. Permission purchase order number: 4590510275279.

Figure 2.7, Feng, B., Weaver, K., Peterson, G.P., 2012, "Enhancement of critical heat flux in pool boiling using atomic layer deposition of alumina", *Applied Physics Letters*, 100(5), Retrieved:<https://doi.org/10.1063/1.3681943>. Permission purchase order number: 4590510373552.

Figure 2.8, Li, S., Furberg, R., Toprak, M.S., Palm, B., Muhammed, M., 2008, "Nature-Inspired Boiling Enhancement by Novel Nanostructured Macroporous Surfaces", *Advanced Functional Materials*, 18(15) 2215-2220, Retrieved:<https://doi.org/10.1002/adfm.200701405>. Permission purchase order number: 4590510630993.

Figure 2.9, Zhang, B.J., Kim, K.J., Yoon, H., 2012, "Enhanced heat transfer performance of alumina sponge-like nano-porous structures through surface wettability control in nucleate pool boiling", *International Journal of Heat and Mass Transfer*, 55(25-26) 7487-7498, Retrieved:<https://doi.org/10.1016/j.ijheatmasstransfer.2012.07.053>. Permission purchase order number: 4590510783129.

Figure 2.10, Ahn, H.S., Kim, J.M., Park, C., Jang, J.W., Lee, J.S., Kim, H., Kaviany, M., Kim, M.H., 2013, "A novel role of three dimensional graphene foam to prevent heater failure during boiling", *Sci Rep*, 3 1960, Retrieved:<https://doi.org/10.1038/srep01960>. Only citation required.

Figure 2.12, Wong, K.K., Leong, K.C., 2018, "Saturated pool boiling enhancement using porous lattice structures produced by Selective Laser Melting", *International Journal of Heat and Mass Transfer*, 121 46-63, Retrieved:<https://doi.org/10.1016/j.ijheatmasstransfer.2017.12.148>. Permission purchase order number: 4590520451324.

Figure 2.13, Chen, R., Lu, M.-C., Srinivasan, V., Wang, Z., Cho, H.H., Majumdar, A., 2009, "Nanowires for Enhanced Boiling Heat Transfer", *Nano Letters*, 9(2) 548-553, Retrieved:<https://doi.org/10.1021/nl8026857>. Reprinted (adapted) with permission from (Chen, R., Lu, M.-C., Srinivasan, V., Wang, Z., Cho, H.H., Majumdar, A., 2009, "Nanowires for Enhanced Boiling Heat Transfer", *Nano Letters*, 9(2) 548-553, Retrieved:<https://doi.org/10.1021/nl8026857>.) Copyright (2009) American Chemical Society.

Figure 2.14, Udaya Kumar, G., Suresh, S., Thansekhar, M.R., Halpati, D., 2018, "Role of inter-nanowire distance in metal nanowires on pool boiling heat transfer characteristics", *J Colloid Interface Sci*, 532 218-230, Retrieved:<https://doi.org/10.1016/j.jcis.2018.07.092>. Permission purchase order number: 4594481217956. "Reprinted from , Udaya Kumar, G., Suresh, S., Thansekhar, M.R., Halpati, D., 2018, "Role of inter-nanowire distance in metal nanowires on pool boiling heat transfer characteristics", *J Colloid Interface Sci*, 532 218-

230, Retrieved:<https://doi.org/10.1016/j.jcis.2018.07.092>., with permission from Elsevier."

Figure 2.15 (I), Deng, D., Feng, J., Huang, Q., Tang, Y., Lian, Y., 2016, "Pool boiling heat transfer of porous structures with reentrant cavities", *International Journal of Heat and Mass Transfer*, 99, 556-568, Retrieved:<https://doi.org/10.1016/j.ijheatmasstransfer.2016.04.015>. Permission purchase order number: 4590520831477.

Figure 2.15 (II), Liter, S.G., Kaviany, M., 2001, "Pool-boiling CHF enhancement by modulated porous-layer coating: theory and experiment", *International Journal of Heat and Mass Transfer*, 44(22) 4287-4311, Retrieved:[https://doi.org/10.1016/S0017-9310\(01\)00084-9](https://doi.org/10.1016/S0017-9310(01)00084-9). Permission purchase order number: 4590520940556.

Figure 2.15 (III), Li, C.H., Li, T., Hodgins, P., Hunter, C.N., Voevodin, A.A., Jones, J.G., Peterson, G.P., 2011, "Comparison study of liquid replenishing impacts on critical heat flux and heat transfer coefficient of nucleate pool boiling on multiscale modulated porous structures", *International Journal of Heat and Mass Transfer*, 54(15-16) 3146-3155, Retrieved:<https://doi.org/10.1016/j.ijheatmasstransfer.2011.03.062>. Permission purchase order number: 4590521048700.

Figure 2.16, Chu, K.-H., Soo Joung, Y., Enright, R., Buie, C.R., Wang, E.N., 2013, "Hierarchically structured surfaces for boiling critical heat flux enhancement", *Applied Physics Letters*, 102(15), Retrieved:<https://doi.org/10.1063/1.4801811>. Permission purchase order number: 4590521134185.

Figure 2.17, Rahman, M.M., Olceroglu, E., McCarthy, M., 2014, "Role of wickability on the critical heat flux of structured superhydrophilic surfaces", *Langmuir*, 30(37) 11225-11234, Retrieved:<https://doi.org/10.1021/la5030923>. Reprinted (adapted) with permission from (Rahman, M.M., Olceroglu, E., McCarthy, M., 2014, "Role of wickability on the critical heat flux of structured superhydrophilic surfaces", *Langmuir*, 30(37) 11225-11234, Retrieved:<https://doi.org/10.1021/la5030923>.) Copyright (2014) American Chemical Society.

Figure 2.18, Dhillon, N.S., Buongiorno, J., Varanasi, K.K., 2015, "Critical heat flux maxima during boiling crisis on textured surfaces", *Nat Commun*, 6 8247, Retrieved:<https://doi.org/10.1038/ncomms9247>. Only citation required.

Figure 3.6, Kandlikar, S.G., 2013, "Controlling bubble motion over heated surface through evaporation momentum force to enhance pool boiling heat transfer", *Applied Physics Letters*, 102(5), Retrieved:<https://doi.org/10.1063/1.4791682>. Permission purchase order number: 4591000515798. Reprinted from [Kandlikar, S.G., 2013, "Controlling bubble motion over heated surface through evaporation momentum force to enhance pool boiling heat transfer", *Applied Physics Letters*, 102(5), Retrieved:<https://doi.org/10.1063/1.4791682>.] with permission of AIP Publishing."